**Title: Efficient pheromone navigation via antagonistic detectors in *Caenorhabditis elegans* male**

**Authors:** Xuan Wan[1,2], Tingtao Zhou*[3,4], Vladislav Susoy*[5], Alessandro Groaz[1,2], Core Francisco Park[5], John F. Brady[3,4], Aravinthan D.T. Samuel[5], Paul W. Sternberg†[1,2].
*These authors contributed equally to this work.
† corresponding author

**Author affiliations:**

1. Division of Biology and Biological Engineering, California Institute of Technology, Pasadena, CA 91125, USA.
2. Tianqiao and Chrissy Chen Institute for Neuroscience, California Institute of Technology, Pasadena, CA 91125, USA.
3. Division of Engineering and Applied Science, California Institute of Technology, Pasadena, CA 91125, USA.
4. Division of Chemistry and Chemical Engineering, California Institute of Technology, Pasadena, CA 91125, USA.
5. Department of Physics and Center for Brain Science, Harvard University, Cambridge, MA, USA

**Corresponding author:** Paul W. Sternberg

**Email:** pws@caltech.edu

**Abstract**

Chemotaxis to a moving potential mate that emits a volatile sex pheromone poses a navigation challenge requiring rapid, precise responses to maximize reproductive success. Volatile chemicals form gradients that differ from soluble compounds, potentially making navigation based on comparisons between spatially separated sensors unreliable for small-bodied animals. Here we show that, rather than a simple spatial comparison, *Caenorhabditis elegans* males employ an antagonistic strategy, comparing inputs from sex-shared head (AWA) and male-specific tail (PHD) sensory neurons with distinct response properties. Despite sharing a receptor, SRD-1, these detectors play different roles: AWAs promote forward movement and acceleration, while PHDs induce reversals and deceleration. In rising pheromone gradients, AWA activity dominates; in falling gradients, AWA inactivates, allowing PHD to correct trajectories. AWAs are essential for mate-searching, while PHDs are crucial for complex tasks. A minimal computational model reproduces these behaviors and infers how head–tail signals are combined. Thus, a sexually dimorphic, antagonistic sensory system enables adaptive navigation in dynamic environments

**Introduction**

For most animals, finding a mate is an essential task and is an especially significant challenge for organisms that rely on volatile pheromones for mate detection, as the potential mate often moves in a complex environment and establishes a fleeting, low concentration pheromone gradient. To obtain a mechanistic understanding of how animals can rise to this challenge, we studied navigation in *C. elegans* as it has a highly accessible nervous system.

Self-fertilizing *C. elegans* hermaphrodites emit a volatile pheromone when sperm are depleted [1-5]. Volatile chemosensory signals are fundamental to facilitating complex behaviors such as strategic navigation, active sampling, and sequential decision-making across diverse species; they are crucial for reproductive success [6-8]. As sex pheromones guide both innate and learned mate-searching activities in many animals, they provide an opportunity to study the neurobiological underpinnings of sexually dimorphic behaviors

[9-18]. For example, the differential responses of males and females to identical stimuli, such as sex pheromones, raise questions about the sensory and neural circuit bases of sexual dimorphism in behavior [19-22].

*C. elegans* produces both soluble and volatile sex attractants. Soluble nematode-specific ascarosides are modulators of social/sexual behaviors and developmental regulation [23-41]. In contrast, this study focuses on a volatile, non-ascaroside sex pheromone (hereafter referred to as "the volatile sex pheromone") that remains chemically unidentified but plays a critical role in sexual communication by signaling fertility and sexual maturity, as it can only be produced by hermaphrodites with no sperm due to depletion or dysfunction [3,42]. As hermaphrodites with no sperm can be considered females we classify this pheromone as a female sex pheromone. The only known receptor for volatile sex pheromone is the G protein-coupled receptor (GPCR) SRD-1, which is expressed in the sex-shared amphid neuron AWA in males only, implying underlying sexually dimorphic sensory processing by that neuron [4].

The complexity of neural circuit questions makes studies in simple models such as *C. elegans* highly useful to rigorously define neural algorithms used by animals. The neural circuitry underlying chemoattraction in *C. elegans* has been mapped with increasing precision, suggesting that sensory neurons process environmental stimuli with remarkable reliability [43]. Besides of the sensitive sensory neurons, it also has a network of interneurons that plays critical roles in processing sensory information and guiding behavioral responses that collectively facilitate navigation and avoidance behaviors: AIA amplifies olfactory signals, AIB controls reversals, AIY mediates response to gradients, AIZ modulates turns, and AVA initiates backward movement [44-52]. These circuits facilitate essential survival behaviors, employing mechanisms such as temporal integration [43], rapid desensitization [53], and the modulation of behavioral responses based on previous experiences and current conditions [44,48,54-65]. In short, the probabilistic nature of behavioral outcomes in *C. elegans* can be traced to the dynamic state of the neural network beyond sensory neurons, potentially explaining the variability in behavior outcomes from identical stimuli in the same individual [54,66].

Previous studies have shown that *C. elegans* employs sensory detectors on opposite ends of its body for rapid avoidance responses to aversive stimuli like SDS, H2O2, and glycerin [67-69], where quick response is prioritized over accuracy. In contrast, our study uncovers a volatile attractant chemotaxis mechanism in which dual detectors are instead used for target searching, a process that demands both rapid responses and high precision to successfully locate the target. Here, we describe a unique attractant dual-sampling algorithm that utilizes controlled expression of a single receptor to achieve sexually dimorphic chemosensory responses and an innate, adaptive navigation strategy for efficient volatile chemical chemotaxis.

In this study, we discover that the male tail-specific neuron, PHD, in addition to AWA, expresses SRD-1 and responds to the sex pheromone as well. We demonstrate that PHD is specifically required for navigation during challenging tasks. Using optogenetics, we compare the contributions of head and tail neurons to behavioral responses. To understand their interaction, we investigate the neural circuitry connecting them, and revisiting their response properties, we find that head and tail neurons detect distinct aspects of the pheromone gradient and concentration. Based on these findings, we propose a computational model to help elucidate navigation strategies.

**Result**

**Volatile pheromone receptor SRD-1 is expressed in PHD, a male-specific neuron in the tail**

Male *C. elegans* sense the volatile female sex pheromone via SRD-1 [4,42], a GPCR. In hermaphrodites, it is expressed only in ASIs in head region and PHAs in tail region. Whereas In males, SRD-1 is expressed in the AWA and ASI sensory neurons in head region. In males, SRD-1 was reported to be expressed in a pair of tail neurons [70,71], which we now have identified as the newly discovered pair of PHD neurons using several transcriptional reporters, based on their location, morphology, and marker gene expression (Figure 1A showing an extrachromosomal array strain (*srd-1P*::mCherry); Figure 2A and S1B showing an integrated cGAL-UAS strain (*srd-1P*::cGAL; UAS::GFP); and Figure S1C showing a marker for Ray B neurons, namely a cGAL-UAS strain *pkd-2*p::cGAL; UAS::GFP; *srd-1P*::mcherry). We further verified SRD-1 expression in PHD neurons using a split cGAL driver with *lin-48d* and *srd-1* 5' transcriptional control regions, where *lin-48* is known to be expressed in PHD neurons [72]. The expression of SRD-1 in PHD neurons was further supported by recent male-specific neuronal transcriptomics data, which revealed heterogeneous SRD-1 expression within these neurons [73]. RNA-seq indicates *srd-1* is detected in ~40% of PHD neurons under standard conditions; however, our integrated *srd-1P*–driven cGAL with UAS::GFP reporter shows uniform PHD labeling (near 100%). Our approach also generated a PHD-specific driver for targeted manipulation of PHD neurons for subsequent experiments (See Figure 2). In *C. elegans* males, AWA is required for chemotaxis towards the sex pheromone [4,42]. While previous studies have linked male tail-specific neuron PHD to various aspects of male behavior [72,74], their specific function remains unclear.

AWA neurons are known to respond to multiple volatile attractants [75-79], whereas PHA neurons are involved in repellent avoidance behaviors [67,76,80], and ASI mediates multiple sensory responses, including repulsion [81]. The sex-specific expression pattern of SRD-1 suggests that the differing behavioral responses to the sex pheromone—strong attraction in males and weak repulsion in hermaphrodites—may result from the sexually dimorphic expression of the chemoreceptor SRD-1. AIn addition, the dual-site expression of SRD-1 in both head and tail neurons suggests that males may integrate SRD-1-mediated sensory inputs from the anterior and posterior regions to navigate effectively toward the volatile pheromone.

**Male-specific PHD is activated by the volatile pheromone**

We next tested if PHD neurons activate in response to the sex pheromone (Figures 1C). We observed that PHD is activated by the sex pheromone from both *C. elegans fog-2* hermaphrodites and *C. remanei* females. To test if this response was mediated via SRD-1, we repeated the experiment in *srd-1(eh1)* loss-of-function mutant males. *srd-1* mutant males showed no PHD activation upon sex pheromone stimulation (Figure 1C). Therefore, male-specific PHD neurons sense volatile sex pheromone via SRD-1. These findings, combined with the known role of PHD in mate-related behaviors [72], suggest its potential involvement in pheromone-guided navigation. Calcium imaging demonstrates that SRD-1 expression in both head (AWA) and tail (PHD) neurons is not merely anatomical but functionally mediates pheromone responses, providing direct evidence that males employ dual detectors to sense pheromone sources.

**PHD neurons enhance mate-searching efficiency in complex environments**

To test the hypothesis that these spatially separated detectors for pheromone actually aid navigation, we used five types of chemoattraction assays designed to represent varying levels of difficulty males might encounter in natural conditions, comparing intact males to those with histamine inhibited-PHD neurons (Figure 2). We achieved specific expression of the HisCl effector (a chemogenetic silencer) in PHD under the control of a split cGAL-UAS line: *lin-48dP*::NLS::cGAL (DBD); *srd-1P*::NLS::cGAL (AD) (Figure 2A). Our experimental design included wild-type (*him-5*) males with/without histamine treatment and PHD-HisCl lines without histamine treatment as controls. Our data showed no significant differences between the three control groups in their response to sex pheromones under all test conditions (Figure 2C-G). Thus,

the observed effects reflect histamine-induced PHD silencing, rather than genetic background or histamine alone.

We first challenged PHD-inhibited males to locate a sex pheromone source placed at the same distance (3 cm) from the source, using two different diameters (6 and 8 cm) agar-filled Petri dishes (Figure 2C, D). PHD-inhibited males refers to males expressing HisCl in PHD via split-cGAL (*lin-48dP*::NLS::cGAL[DBD]; *srd-1P*::NLS::cGAL[AD]) crossed to 15×UAS::HisCl::SL2::GFP and exposed to 10 mM histamine (see Methods). All males located the source within 30 mins. PHD-inhibited males performed as effectively as controls at both distances, indicating that tail neuron input is not essential for simple, close-range navigation tasks. By contrast, when we increased the distance and placed males 5 cm from the source in an 8 cm-Petri dish (Figure 2E), all test subgroup males were unable to locate the source.

We then tested males' ability to locate a more dilute odor. We diluted the sex pheromone concentration 10-fold and observed the responses of histamine-treated/untreated wild-type male (*him-5* male), histamine-treated/untreated PHD-specific driver with HisCl effector males (Figure 2F, S2A). PHD-inhibited males exhibited notable difficulties in identifying the diluted pheromone source, unlike the three control group males. This differential response underscores the essential role of male tail PHD neurons in navigating toward weak pheromone signals.

To understand the effects of increased distance versus stimulus dilution, we conducted Finite Element Simulations of the pheromone concentration field (Figure S3). In our assay setup, the stimulus was placed on the lid of the plate that was half-filled with agar, creating a bi-layer distribution of the pheromone. As illustrated in Figure S3A, the volatile component diffuses rapidly in the air, while the agar absorbs and then slowly releases the volatile component. The concentration field simulation revealed that in experiments where males were positioned far away from the pheromone source, they encountered areas of low absolute concentration without a clear gradient. Conversely, when males were tested nearer to a diluted pheromone source (3 cm), their performance, while reduced relative to controls, was better than in the 5 cm experiment, likely because the diluted source still produced a weak but discernible Gaussian gradient despite its overall low concentration (Figure S3B). These findings suggest that the concentration gradient plays a crucial role in guiding males to the pheromone source.

Since *C. elegans* navigate through three-dimensional (3D) soil and rotting fruit in their natural habitat, we examined the efficacy of PHD-inhibited males in a 3D search paradigm using gellan gum gel (see Methods), which likely better mimics natural conditions than a 2D Petri dish surface (Figure 2G, H). In this endpoint assay, we recorded the number of worms that reach the target spot every 5 minutes. Worms must stop moving at the exact 3D location (depth included) of the pheromone to count as finding it. Control and test droplets are placed at the same depth to control for vertical bias, avoiding confounding from a preference for movement toward the surface or bottom. PHD-inhibited males had reduced proficiency in identifying pheromone sources within 3D spaces, underscoring the importance of PHD neuron inputs for environmental navigation that mirrors natural conditions (Figure 2G, S2A).

Analysis of the distribution of males at multiple timepoints after the addition of stimulus revealed a uniformly low chemotaxis index for the PHD-inhibited male group across all intervals in weak signal and 3D exploration tasks (Figure S2B). In our 2D experiments involving weak signals, most control males successfully located the target within 10 minutes. However, in 3D exploration tasks, the peak arrival time at the target extended to a significantly longer 20 minutes (Figure S2C). Notably, we observed distinct impairments in the navigational behaviors of PHD-inhibited males between weak signal detection and 3D spatial exploration tasks. In weak signal detection, the low chemotaxis index resulted from an equal

distribution of males reaching both the test and control spots. Conversely, in 3D searching tasks, the low chemotaxis index stemmed from fewer males reaching both spots (Figure S2B-D).

**Optogenetic dissection of SRD-1 positive neurons and PHD neuron's roles in male locomotion**

To examine the effects of head versus tail SRD-1 positive neurons on sex pheromone-induced behavior, we used the red-shifted Chrimson variant of channelrhodopsin [82]. We first evaluated the UAS::Chrimson effector driven with a pan-neuronal cGAL driver , demonstrating the system's efficacy (Figure S4A): worms temporarily ceased movement during light stimulation, promptly resuming normal behavior once the light was switched off.

We then activated all SRD-1 positive neurons with Chrimson expressed under the *srd-1* regulatory control, using an *srd-1P* cGAL driver (Figures 3A ATR- and S4C ATR+). The absence of ATR served as a control to negate any potential effects of light alone, confirming that the observed changes in speed were attributable from targeted neuron activation. Under ATR+ conditions (Figure 3A), males exhibited continuous forward movement throughout the 12.5s light stimulation period, transitioning to rapid steering or reduced speed after stimulation ceased, but not in ATR- males (Figure S4C).

To further confirm the role of SRD-1-positive neuron stimulation in modulating locomotor behaviors, we investigated the effects using extended stimulation protocols (30s or 60s light-on intervals followed by 10s light-off intervals) (Figure 3C). During prolonged stimulation, forward movement was sustained, while turning behaviors remained consistently suppressed. Also, the cessation of stimulation was associated with reduced movement speed and an increase in turning rate, consistent with observed dynamics under shorter stimulation conditions.

Using an *odr-10P* cGAL driver crossed to a UAS::Chrimson effector, optogenetic activation of AWA in both sexes produced no detectable behavioral change, indicating that AWA activation alone does not drive forward locomotion or that *odr-10P* cGAL driver yielded insufficient Chrimson expression for activation (Fig. S4B).

We next targeted PHD neurons exclusively. Using a split cGAL driver under the control of *lin-48d* and *srd-1* promoters, we achieved PHD-specific Chrimson expression (Figures 3B ATR+ and S4D ATR-). Under the ATR+ condition, PHD activation in males elicited a decline in average speed throughout the red-light stimulation period, after which males resumed movement. Under matched light stimulation, ATR− males exhibited no effect. This result contrasts with the overall movement patterns observed upon and after the activation of all SRD-1 positive neurons (See Figure 3A). Previous studies also suggest that PHD neurons have a potential role in maintenance of backward locomotion during the mating partner body scanning [72]. We also observed that repeated activation of PHD neurons also resulted in a gradual reduction in speed (See Figure 3B right panel), suggesting a persistent slowdown effect on locomotor behavior after activation.

Since we also observed behavioral responses to light stimulation in hermaphrodites, we performed a quantitative analysis to distinguish the robustness of these responses in hermaphrodites and males (Figure 3). Hermaphrodite responses were more variable upon optogenetic activation, as also seen in the average speed (Figure 3c) and Fourier analyses (Figure 3d). Fourier analysis of total speed during SRD-1-positive PHD neuron stimulation revealed prominent peaks at 0.05 Hz and 0.025 Hz, corresponding to the 20 s and 40 s stimulation protocols, respectively (Figure 3d). The amplitude and sharpness of the spectral peak at 0.05 Hz (or 0.025 Hz) quantifies the strength of the signal, i.e., the consistency and robustness of the behavioral response to periodic stimulation, and it is consistently stronger in the males' response than the hermaphrodites' by about a factor of two. Hence, we concluded that males display a more robust response.

The more variable response in hermaphrodites also manifested as larger inter-individual differences, as shown by comparing the error bars (shaded area) in Figure 3c in the left two panels. Both these analyses suggest a sex-specific effect of SRD-1-positive neuron activation. Upon PHD neuron stimulation, the male also showed a variable response.

**Head and tail neurons mediate distinct micro-behavioral responses to optogenetic activation**

To confirm and further investigate how activation of SRD-1 positive neurons in the head versus the tail affects behavior, we optically targeted either the head or tail of freely moving males expressing *srd-1* Chrimson cGAL-UAS.

Initial observations showed that males predominantly moved forward in the absence of stimulation (ATR– controls; see Figure 4, S4 and S5), so a short observation window could lead to a false positive result on forward movement. To evaluate the duration and persistence of this response, red light is applied to head region for 30s (Figures 4A). As shown in Figure 3, tail stimulation primarily induced reversals, a rapid transition from forward to backward movement. For the tail region stimulation, we chose short and repeated pulses alternating every 2s over a 15-cycle period to capture multiple reversals (Figure 4A).

After postprocessing, we divided the recording into 2-second segments. For each 2-second segment, we tabulated the behavioral motif displayed by the male or the first behavioral transition that occurred during that segment. We used two complementary behavioral classification frameworks to capture distinct aspects of locomotion dynamics. Four-Motif Analysis (Figure S5) focuses on core locomotion states (forward, backward, forward-to-backward transition, backward-to-forward transition) to highlight macro-level movement changes during head/tail stimulation. Six-Motif Analysis (Figure 4) expands categorization to include nuanced behaviors like self-exploratory (where the worm attempts to probe its own body) and high-frequency direction transitions (marked by frequent direction changes within the 2-second window), which better capture micro-behavioral variability.

A short light pulse delivered to the tail region induced a transition from forward to backward movement, accompanied by increased directional hesitation (Figure 4B). During these hesitant periods, males frequently switched between forward and backward locomotion. However, we observed substantial individual variability in response to tail stimulation. While most worms reliably responded to light stimulation and for 7 pulses, they responded an average of 4.3 times. A subset completely ignored the stimulus. This behavioral heterogeneity may arise from the variable expression of SRD-1 in PHD neurons [73].

With 30 seconds of head stimulation, we noted behaviors analogous to those from activating all SRD-1 positive neurons, including persistent forward movement during light exposure followed by rapid directional adjustment (Figures 4C, S5C). We also observed that after head stimulation, males exhibited self-exploratory behavior (Figure 4C), using their tails to probe against their bodies, a behavior that can persist for several minutes.

**Circuit that combines head and tail inputs to control locomotion direction**

The male connectome [83] suggests locomotion command neurons are the likely locus of integration of the head and tail inputs. Specifically, PHDs have strong connections to PVN (ROI1) and EF (ROI2) interneurons [83] (See Figure 1B), which connect to pre-motor command neurons. The direction of locomotion is controlled by reciprocal inhibition of forward and reverse command neurons [44,50,84,85]. To investigate the circuitry between sex pheromone sensory neurons and these motor command neurons, we specifically activated SRD-1 positive neurons with Chrimson and monitored pan-neuronal calcium dynamics using

GCaMP6s (Figure 5A-C, see Method). SRD-1 positive neurons, including PHD, AWA, and ASI neurons in males, had robust responses to light stimulation (Figure 5C). In addition, two groups of neurons within the male tail region—presumably a pair of PVN neurons in one region of interest (ROI1) and a single EF neuron in ROI2 (Figure 5B-C, S6)—had a strong positive correlation with PHD activity in ATR+ and not in ATR- males (Figures S7). Here, we used normalized activity for regions of interest (ROIs) to facilitate comparison across populations of neurons with varying baseline fluorescence, while raw activity was analyzed for single neurons to preserve their intrinsic activity dynamics and avoid potential distortions from normalization. In the male head region, we observed a more negative correlation with light stimulation. About 4 neurons in the head region are positively correlated with AWA neuron activity and about 10 neurons are negatively correlated (Figure S7).

We observed a strong negative correlation between the activity of the reversal command neurons (AVA) and SRD-1-positive neurons in the head region (AWA and ASI). Although this inverse relationship was also present in the ATR-untreated control group, it was less pronounced. In ATR-untreated worms, the decrease in AVA activity may have been influenced by factors such as movement of the microscope objective or non-specific light responses.

**AWA and PHD have distinct response properties**

It has been suggested that AWA neurons adjust their response based on fold-changes in odor concentration, reducing turning behavior with minimal increases in odor concentration [53]. We used prolonged, behaviorally relevant high concentration sex pheromone stimulation with a thin layer micro-diffusion (TLMD) unit (Figure S8A, see Method), facilitating pan-neuronal calcium imaging (Figure 5D and E) [4]. As shown in Figure 5D, upon pheromone application, AWA and ASI neurons showed immediate calcium influx followed by rapid desensitization to a low, steady state within 1.5 mins, maintaining this level for at least 5 mins. This pattern indicates robust desensitization to even relatively high pheromone concentrations. PHD neurons exhibited sustained activation for at least 9.5 mins with a gradual decline, indicative of their threshold-sensing properties (Figure 5E). 62.5% of imaged males exhibited a rapid response to pheromone exposure and sustained high levels of activity, whereas the remainder displayed a slow response, with delayed activation (2.5 mins post-stimulus) with a 40% reduced calcium signal amplitude (Figure 5E, cropped to 250 second; D, full length 600 second). The fast and slow responses of PHD neurons are particularly intriguing. Recent male neuron transcriptomics data revealed a heterogenetic expression of SRD-1 in male PHD neurons, which may result in this individual variation [73]. This pattern may also be caused by PHDs being actively inhibited by other neurons. According to the connectome, PHDs are post-synaptic to several neurons [83], which may modulate their activity and contribute to the observed variability in response dynamics.

During the initial phase of neuronal activity, before the activation of PHD neurons, pheromone-stimulated calcium imaging revealed a negative correlation between reversal command neurons (AVA and AVE) and head sensory neuron activities (AWA and ASI) (Figure 5D). This negative correlation suggests that the inhibition of reversal command neurons by head neurons is pivotal for forward movement during gradient ascent. As demonstrated by the set of optogenetic experiments (see Figure 3 and 4), gradient-sensing neurons in the head region dominate PHD input and primarily drive forward movement, suggesting that head neuron activity may override tail neuron activity.

In the subsequent phase of neuronal activity, AWA and ASI activity became hyperpolarized, and all PHD neurons were activated. This allowed us to examine the direct correlation between PHD neurons and reversal command neurons (AVA and AVE). We observed that reversal command neurons exhibited a negative correlation with head sensory neurons and a positive correlation with tail sensory neurons (PHD)

(Figure 5F), suggesting PHD-mediated activation of reversal command neurons, consistent with the observed reversal behavior during optogenetic activation (see Figures 3, 4).

**PHD and AWA neurons drive AVA activity at distinct concentration thresholds**

To confirm the correlation between reversal command neurons and anterior and posterior SRD-1-positive neurons in different sex pheromone concentrations, and to determine the concentration threshold for behavior changes, we fabricated a head and tail multi-inlet microfluidic chip (Figure 6A). We utilized immobilized worms within microfluidic chips to precisely control the delivery of varying concentration stimulations to the head or tail independently. This setup enabled accurate stimulus application to distinct regions and facilitates switching between a control buffer and three different stimulus concentrations.

*C. elegans* has five pairs of premotor command interneurons, two of which promote forward locomotion and three of which promote reverse locomotion. These groups are interconnected and control distinct motor neurons [44,50,84,85]. AVA neuron activity peaks at the start of a reorientation [44,49,50,52,84] and AVA interneurons integrate opposing signals from head and tail sensory neurons, guiding behavior [68,86]. AVA's diverse activities across time scales position it as a key neuron in coordinating forward and backward movements [68,86]. Therefore, monitoring AVA neuron activity provides a useful indicator of the animal's forward and reversal behaviors.

Using diacetyl as a baseline attractant to validate our device (Figure 6B-b), we observed that all tested concentrations led to decreased AVA neuron activity, suggesting an enhancement of forward movement. Diacetyl at higher concentrations more effectively suppresses AVA neuron activity. We then tested pheromones at varying concentrations applied to both ends and separately to the head and tail (Figure 6B-c). Simultaneous stimulus of both ends immediately decreased AVA activity, indicating forward movement. Remarkably, head-only stimulation caused a greater reduction in AVA activity compared with stimuli to both ends, whereas tail-only stimulation resulted in increased AVA activity (Figure 6B-d,e); this difference suggests antagonism of head and tail input, consistent with our optogenetic and sex pheromone stimulation calcium imaging showing that head neurons activation promotes forward movement and tail PHD neuron activation triggers reversal (see Figures 3, 4 and 6Ba). These increases and decreases in AVA activity only last for one minute.

We performed area-under-curve (AUC) analysis on the AVA neural activity data (See Method). Notably, SRD-1 positive neurons in the head and tail show different preferences for sex pheromone concentrations. Higher pheromone concentrations more effectively suppress AVA activity when applied to both ends or exclusively to the head (Figure 6Bc-d). In contrast, AVA activation peaked at pheromone dilutions of 100–500X when applied only to the tail (Figure 6C). But, at dilutions of 500X, 1000X, and 2000X, AVA neurons displayed predominantly random oscillations when pheromones were applied to the head or both ends (Figure S10D). These findings suggest that higher pheromone concentrations promote forward movement more effectively, with head neurons strongly inhibiting AVA activity and weaker tail neuron activation contributing to sustained forward movement and increased speed. At low concentrations, the inhibition from head neurons diminishes, and tail neuron activation becomes more prominent, reducing forward movement. We also noted significant spontaneous oscillations in AVA neuron signals across individuals, a finding shown in similar studies using microfluidic chips [66,87,88]. These fluctuations are likely due to the inherent spontaneous oscillation nature of AVA neurons, individual animals' internal status, and the restrictive environment of the microfluidic channels, which may discomfort the worms and trigger attempts to escape, causing variable AVA neuron signal patterns.

**Command neurons integrate antagonistic inputs from the head and tail**

The integration of inputs from SRD-1-positive neurons in the head and tail regions reveals a sophisticated signal-processing algorithm that optimizes navigation. Optogenetic stimulation data (Figures 3, 4) demonstrate that activation of tail-region neurons induces reversal behavior and slows locomotion, while stimulation of head-region neurons suppresses turning, promotes forward locomotion, and increases speed. Notably, head-region activation alone mimics the effects of activating all SRD-1-positive neurons, highlighting the dominant role of anterior SRD-1-positive neurons in guiding behavior. This aligns with findings from AWA-defective *odr-7* mutants and AWA laser-ablated males [4,42], where AWA neurons are critical for locating pheromone sources, while ASI and PHD neurons are insufficient on their own. Conversely, the absence of tail-region PHD neurons impairs pheromone localization under natural, complex conditions, though it has minimal effects in ideal laboratory settings with high pheromone concentrations, reduced noise, and simpler navigation challenges (Figure 2C, D). Together, these data suggest a dual-detector system in males integrating head and tail neurons' sensory input, with tail neuron activation acting as a corrective mechanism during navigational errors to enhance chemotaxis efficiency.

Pheromone stimulation calcium imaging data further elucidates this integration (Figure 5D). By fitting AVA neuronal activity into a linear model incorporating AWA and PHD activity, the best-fit equation has AVA activity = −0.7 × AWA activity + 0.1 × PHD activity − 0.2, indicating that AVA responses are primarily driven by inhibitory input from AWA neurons in the head, with a smaller excitatory contribution from PHD neurons in the tail (Figure 5F).

Microfluidics chip-based experiments (Figure 6D) further validated this integration mechanism. The area under the curve (AUC) of AVA neuron activation during head-specific and tail-specific stimulation closely matches the trends observed with dual stimulation. This suggests that the neuronal response results from a combination of antagonistic inputs from head and tail regions, providing a computational framework for navigating pheromone gradients. This dual-system integration reflects a sex-specific chemoreceptor-driven behavioral adaptation for efficient navigation in complex environments.

**A simple computational model for spatially separated detectors navigation in *C. elegans***

Sensory neuron inputs are typically conserved through the connectome and determine the behavioral outcomes [53]. Summarizing the experimental observations of the strong correlations between the AWA, PHD and AVA neurons (Figures 5, 6), we propose a simple model to demonstrate the roles of head and tail sensory inputs. We focused on macroscopic navigation behavior and neglected details of microscopic traits and changes in worm body curvature in motion.

*C. elegans* exhibits a remarkable ability to navigate complex environments using chemical cues. Two established directional navigation strategies have been observed [76,89-94]: (1) Klinokinesis, a random walk biased toward the stimulus, such as in bacterial chemotaxis, requires comparing concentrations over time to adjust random turning that lacks directionality towards the correct heading. (2) Klinotaxis, a more refined navigation, utilizes directional turns to achieve more accurate gradient navigation [89,95-98]. Here, we modeled kinesis and taxis separately.

During kinesis searching, we modeled locomotion as a mixture of active Brownian motion [99] and run-and-tumble motion [100] (see Methods). Our first key assumption is that sensory inputs from the head and tail are converted into confidence variables $Q^H$ and $Q^T$, which then determine the worm's dynamical state (Figure 7A). As the activity of reversal command neurons AVA and AVE is found to correlate negatively with

AWA activation but positively with PHD neuron activation, we propose a simple form to qualitatively capture these correlations:

$$\gamma = \gamma_0 e^{-\lambda_K (Q^H - Q^T)},\ U = U_0 + U_1(Q^H - Q^T + \eta). \quad (1)$$

Here $\gamma_0 = 0.067/s$ is the baseline tumbling rate. $U_0 = 0.064$ mm/s is the baseline average speed, and $U_1 = 0.03$ mm/s is the magnitude of speed fluctuation. $\lambda_K$ represents the strength of klinokinesis, and $\eta$ represents a Gaussian noise in the speed. The worm's dynamic state is characterized by its speed and tumble rate $(U, \gamma)$. Loss of AWA or PHD input disrupts $Q^H$ or $Q^T$ computation, leading to impaired speed and turning regulation. The equations for $(U, \gamma)$ connect the non-directional kinesis movements to confidence variables from head and tail inputs, which are subcircuit responses to stimuli on the head and tail sensory neurons. These mechanisms are also known as orthokinesis (for $U$) and klinokinesis (for $\gamma$).

Our model is based on the idea that sensory information coming from the worm's head and tail is translated into a signal that is a measure of 'confidence' ($Q$), and these signals directly determine the worm's behavior and movements (Figure 7A). AWA neurons become more active as sex pheromone concentration increases [4]. In our microfluidics chip-based experiment, we found that input from head neurons suppressed AVA neuron activity (Figures 5, 6B-d). Therefore, in our model, the confidence signal based on head input ($Q^H$) will rise with increasing pheromone concentration until it reaches saturation (see blue line in Figure 7A). Interestingly, high pheromone concentrations applied to the tail suppress AVA neuron activity, in contrast to the activation observed at low concentrations (Figures 5, 6B-e). Furthermore, continuous activation of the PHD neuron will result in a reduction in baseline speed and the sprint behavior exhibited upon proximity to the target, suggesting that $Q^T$ should decrease below zero to capture these observations (see red line in Figure 7A). We propose using the $Q^H - Q^T$ model (see purple line in Figure 7A) to represent the negative correlation between AVA/AVE command neurons and AWA activation, and the positive correlation with PHD neuron activation. Importantly, only $Q^H - Q^T$ accurately captures the observed increase in speed towards the end of navigation, which wouldn't be captured by simply adding the two signals together (compare purple and green lines in Figure 7A).

To determine the dynamics of $Q^H$ and $Q^T$ given external concentration field evolution, we adopt the simplest dynamics model with a single memory timescale:

$$\frac{dQ^H}{dt} = -k_1 Q^H + k_2^H f_H\left(C, \frac{dC}{dt}\right), \quad (2)$$

$$\frac{dQ^T}{dt} = -k_1 Q^T + k_2^T f_T(C).$$

Here $\frac{1}{k_1}$ is the timescale of memory, while the values of $k_2^{H,T}$ represent the sensitivity of SRD-1 positive neurons. $f_H$ and $f_T$ represent the sensory inputs, and they are chosen to qualitatively reflect the observations in this work and AWA calcium dynamics in [53] (see Methods). Key assumptions are: (1) the long decay time of PHD activity level during constant sex pheromone stimulation, as seen in Figure 5F, indicates that PHD sensory input mainly depends on the absolute concentration. Hence, $f_T$ is only a function of $C$. (2) PHD response is positive at intermediate concentration ranges but becomes strongly suppressed at high concentrations, as shown in Figure 6C. (3) The relatively short decay time of AWA activity level during constant stimulation, as shown in Figure 2 of ref [53], indicates that AWA sensory response mainly reflects the detected concentration change, with a mild increase as absolute concentration increases. For simplicity, in this model worms will make directional (taxis) turns when they (1) detect a high enough concentration above a threshold value, and (2) if they currently experience a decrease in concentration. Such turns are assumed to be perfectly accurate toward the source direction. Based on our experimental observations, head-inhibited worms will not perform taxis turns.

We performed simulations for navigation on a small Petri dish with the concentration simulation for 30 mins (Figure 7B). Each simulation contains 10000 worms, initialized with random orientations. When both head and tail sensory inputs are missing, $Q^H = Q^T = 0$, the worms perform a standard active random walk with constant mean speed and tumble rate (Figure 7C). Only a small fraction – about 10% of worms – were able to find the pheromone source by luck, as seen in the grey curve of Figure 7D and Supplementary Movie 2.

Adding tail sensory input alone significantly enhanced the chance of finding the pheromone source, almost doubling the probability (Figure 7D light blue curve). Adding head sensory input boosts the overall success rate to nearly 100%, simply due to the dominating effect of taxis turns (Supplementary Movie 1). Overall, with tail input, the trajectories are biased closer to the pheromone source, as shown in Figure 7E and S11. In each simulation, worms start from a small region around the center of the plate and the pheromone source is located at the red point on the left side. We denote the direction from the pheromone source to the plate center as the x direction and measured the average x position of all worms during the entire simulation. This is denoted as <x> on top of each panel in Figure 7E. We notice that <x> is negative whenever tail input is present but becomes positive when tail input is absent. Hence, tail input enables worms to move on average to the left side of the plate, i.e., they behave more attracted to the pheromone source with tail inputs. We compute the maximum distance from the pheromone source that reaches worm reaches during the search, denoted as $d_{max}$. For successful worms with head inputs, the addition of tail input accelerates their search so that their $d_{max}$ is slightly smaller compared with those without tails. In the absence of either head or tail inputs, worms only perform random walks and stay near the starting position; adding tail input effectively incentivizes them to explore larger areas and be more biased to the source, manifested in significantly larger $d_{max}$ values. Overall, these simulations suggest that tail input significantly improves the success rate of mate-searching.

## Discussion

### Computational modeling suggests tail input suppresses mistakes

Building on our computational modeling of pheromone diffusion, we find that tail input is essential for suppressing navigation errors arising from the rapid diffusion of volatile attractants. Specifically, our finite element method (FEM) simulations reveal that the pheromone concentration field deviates from Gaussian distributions, and based on our simulations of the dynamical model, the resulting pheromone distributions can lead to artificial increases in head confidence $Q^H$ for worms in low concentration regions due to the finite plate size, leading to erroneous behaviors without tail input. Compared to water-soluble chemicals studied previously, air-borne pheromones diffuse rapidly, creating a nonlinear process where the agar initially absorbs pheromones to a high concentration before emitting them back into the air. This non-Gaussian behavior is characteristic of chemicals transported across air and agar phases and must be considered in chemotaxis models.

The errors caused by artificial increase in head confidence can be mitigated by the tail. Tail input corrects these errors by increasing the tumble rate, ensuring more efficient directional adjustments. Moreover, suppressing PHD activity at high concentrations $Q^T \to -1$ significantly improves navigation, supported by GCaMP data showing reduced PHD activity under 1x concentration stimulation (Figure 4). Consequently, we adopted a functional form for PHD response: $\lim_{C\to 0} Q^T \to 0$ , $\lim_{C\to C_0} Q^T \to 1$ , and $\lim_{C\to \infty} Q^T \to -1$. These dynamic properties suggest that the interplay between head and tail neurons is critical for robust navigation strategies, offering an extensible framework for modeling chemotaxis in complex environments.

Critically, our simulations also revealed that the concentration differences between anterior and posterior positions are negligible due to the small size of the worms. This fundamental constraint necessitates an alternative navigation strategy: rather than measuring spatial differences along the body axis, *C. elegans* employs antagonistic comparison between functionally specialized head (AWA) and tail (PHD) neurons. This computational innovation allows robust navigation where traditional gradient sensing would fail.

**Sexually dimorphic decision-making in *C. elegans* stems from sensory neuron inputs**

The distinct responses of males and females to the same sex pheromone prompt questions about the neural foundations of behavioral sexual dimorphism [3,4,42]. Our findings indicate that sexual dimorphism in naïve *C. elegans* males' response to sex pheromone stimulation stems from variations in receptor expression. This leads to differential sensory neuron activity propagating through neural circuits, culminating in distinct behaviors. Although existing data from other organisms suggest that sex-specific pheromone responses arise from sexually dimorphic neural circuits rather than differential sensory perception [9,101,102], incomplete characterizations of neural networks in more complex model organisms may bias our interpretation of this phenomenon. *C. elegans* exemplifies an olfactory system where sophisticated modulation of a single receptor's expression allows both efficient chemotaxis and the execution of distinct sex-specific behaviors. Therefore, the behavioral outcomes in naïve animal during navigation can be predicted from activity of the key sex pheromone sensory neurons.

PHD neurons remained active for ⩾9.5 min with a slow decay (Figure 5E). Across animals, responses segregated into two classes: fast responders (62.5% of males) showed an immediate, sustained increase at pheromone onset, whereas slow responders (37.5%) exhibited a ~2.5-min delay and ~40% lower peak ΔF/F. Two non-exclusive mechanisms could underlie this heterogeneity. (1) Molecular variability: single-cell datasets report variation in *srd-1* abundance in PHD. Although both of our cGAL–UAS reporter lines labeled PHD uniformly (~100%), cGAL–UAS amplification can mask modest expression differences; thus, the heterogeneity is likely quantitative (more vs. less SRD-1) rather than all-or-none. Moreover, single-cell/single-nucleus RNA-seq can under-detect low or intermittent transcripts due to limited capture efficiency and technical dropouts/zero inflation—issues known to disproportionately affect sparsely expressed GPCRs [103-107]. (2) Circuit gating: PHD receives postsynaptic inputs from multiple neurons; state-dependent inhibition from these partners could delay onset and reduce amplitude in some animals. We therefore interpret the fast/slow classes as reflecting threshold-sensing in PHD modulated by receptor dosage and/or inhibitory factors. Discriminating between these mechanisms will require targeted experiments (e.g., *srd-1* dosage manipulations and selective silencing of candidate presynaptic partners during PHD imaging).

**Decision in uncertainty: how worms navigate complex gradients with imperfect sensory input and inaccurate steering angle control**

As a complementary approach to experimental observations of the worms' turning behaviors, we conducted mathematical analysis for the optimal turn angle and compared it for consistency with our observed data. We modeled an idealized worm with precise short-term memory of its trajectory and the ability to precisely detect concentration gradients in its path by traveling along the same direction for a short duration. We assume that the ideal worm's sensory systems are infallible, and the worm's neural circuitry can process this information, such that sampling along two distinct directions will be theoretically sufficient to identify the gradient's direction. In practice, however, a non-ideal worm's memory and sensory perception are inaccurate due to inherent noise, complicating the task of gradient estimation. This challenge mirrors a regression problem where the objective is to select an optimal turning angle for a second sample that minimizes the uncertainty in determining the gradient's direction. We assumed a

steady concentration field that does not vary with time during the sampling of two directions of a non-ideal worm.

Our analysis for a non-ideal worm, grounded in a least-squared-error regression framework, suggests that the optimal choice for a second sampling direction consistently exceeds 90 degrees regardless of the initial sampling orientation relative to the actual gradient direction. With an initial orientation distributed uniformly randomly, the preferable turning angle is approximately 120 degrees (Figure S12). This direction is chosen to be away from the gradient if the initial angle is qualitatively aligned (less than 90 degrees from the gradient) and towards the gradient otherwise. Given the worm's lack of precise knowledge of gradient direction, it faces a choice: turn 120 degrees in either direction or, as a compromise, nearly 180 degrees (Figure S12). Observations suggest that worms likely opt for turns close to 180 degrees in early search stages, indicating a strategic approach to maximize information gain about the gradient's direction. Worms thus intricately balance their behavioral strategies with their sensation, motor control, and cognitive limitations.

**A navigation strategy based on an integrative dual-detector mechanism**

Dual detectors to control directional movement allow simultaneous comparison of stimulus rather than a single organ comparison in time. In *C. elegans*, the phasmid neurons in the tail, similar to the amphid chemosensory organs in the head, perform a chemosensory function [67]. Indeed, amphid and phasmid neurons influence the worm's backward movements when exposed to repellents, integrating sensory inputs from both the head and tail to promote effective escape behaviors [67,69,108]. The AVA interneurons consolidate signals from the head and tail sensory neurons to steer behavioral choices [108]. Our study provides evidence of dual detectors in attractant navigation. Repellents demand rapid avoidance (reversal), while attractant sensing requires complex, targeted navigation strategies.

For repellent avoidance behaviors, worms employ a simple strategy in which both head and tail inputs trigger reversal [67,69,108], distinguishing it from the more complex mechanisms underlying attractant navigation. In attractant navigation (Figure 8), head- and tail- located neurons utilize the same receptor but drive distinct and opposing sensorimotor responses: 1) AWA promotes forward movement and speeding up while PHD induces reverse movement and slowing down. 2) Behavioral output is typically dominated by AWA activation, while PHD input provides antagonistic modulation of AWA-driven behavior. 3) The head neuron exhibits gradient-sensing properties and rapid desensitization in constant concentrations, while the tail neuron displays threshold-sensing properties and remains activated under constant concentrations. 4) PHD neurons are activated at lower pheromone concentration, thus preventing males from making false taxis turns induced by rapid temporal evolution of volatile pheromone concentration. PHD neurons are inactive at high pheromone concentration, promoting rapid acceleration (sprints) as the male approaches the pheromone source. We computationally modeled the response, proposing that males have a measure of confidence that they are proceeding in the right direction; the absence of PHD input disrupts directional confidence, preventing the acceleration response. This demonstrates a fundamental aspect of neural circuitry: different neurons have evolved to handle distinct environmental stimuli.

Contrary to prior hypotheses [109-112], *C. elegans* does not rely solely on simple head-tail concentration comparisons but instead employs a more complex antagonistic mechanism involving head and tail sensory neurons, each with distinct preferred concentrations for optimal activation. Our proposed mechanism focuses not on the spatial separation of receptors but on comparing signals from two distinct sensory neuron types, AWA and PHD, with different response properties. This comparison enables the animal to integrate various aspects of pheromone gradient dynamics and make adaptive behavioral decisions. While

the mechanism relies on comparing outputs from these neurons, their differences stem more from their response characteristics rather than their physical locations. This strategy would be particularly beneficial for navigating a volatile gradient, such as a shallow and low-concentration pheromone gradient, where there is minimal difference in concentration between the worm's head and tail, making head-tail absolute concentration comparisons very unreliable.

To assess whether spatial separation between AWA (head) and PHD (tail) produces a concentration disparity in what they sense, we quantified the relative difference $|C(\text{head}) - C(\text{tail})| / C(\text{body})$ ($C$, concentration) across our concentration field simulated arenas (Fig. S3C). Specifically, we computed this metric and then averaged over (1) the full plate area, (2) the entire simulation duration, and (3) all worm orientations $\theta \in [0,2\pi]$. The resulting empirical distribution is strongly concentrated near zero (probability density shown on a log scale), with a 99th percentile of 0.1056. Thus, for >99% of space-time-orientation, $|C(\text{head}) - C(\text{tail})| / C(\text{body}) < 0.1056$. The rare larger values arise predominantly near plate edges where $C$ is itself very small and the ratio becomes numerically noisy, rather than reflecting meaningful signal gradients.

Consistent with this result, our model already incorporates stochasticity in head and tail confidence. Across relative noise magnitudes of 0.01–0.1, model outputs changed minimally. Because the typical head–tail concentration contrast is of the same order or smaller than this noise amplitude, we do not expect it to carry reliable information for navigation under our conditions. These quantitative results justify our simplifying assumption to ignore explicit head–tail concentration differences in the main model without altering the qualitative conclusions.

Besides our work, other studies have shown that numerous chemosensory GPCRs are also co-expressed in the head amphid and tail phasmid neuron classes [67,113-116], which raises the possibility that this antagonistic detector mechanism may represent a general strategy in *C. elegans* navigation. This mechanism, integrating distinct neuronal responses to environmental stimuli, allows precise adaptation to dynamic and complex sensory landscapes. Beyond pheromone navigation, the principles uncovered here likely extend to other volatile chemosensory contexts, providing a broader framework for understanding how animals solve the universal challenge of searching for moving targets within noisy and variable environments.

## Methods

### Worm Strains

Strains of *C. elegans* used in this study originated from the N2 (Bristol) wild-type lineage and were maintained under standard laboratory conditions using Nematode Growth Medium (NGM) plates with *E. coli* OP50 as the food source. Detailed information regarding the strains is provided in Supplementary Table 1.

### Statistics & Reproducibility

All experiments were performed on *C. elegans* adults, with individual worms treated as independent biological replicates. Sample sizes were chosen based on prior work in the field, pilot experiments, and practical considerations (e.g., expected behavioral variability and assay throughput), and are reported in the figure legends and/or Methods for each experiment. No statistical method was used to predetermine sample size. For tracking-based optogenetics assays, trajectories were excluded using pre-established quality-control criteria: worms were excluded if they physically contacted another worm during the assay

657 or reached the plate edge; across ~150 imaged worms per sex, ~120 trajectories passed quality control
658 and were analyzed. Outside of these pre-defined criteria, data exclusion is stated explicitly where
659 applicable. Statistical analyses (including curve fitting and linear regression where used) were performed
660 using custom analysis code, and the specific statistical tests, exact n, definition of center and error bars/box
661 plots, and significance thresholds are provided in the corresponding figure legends. The behavior
662 classification were randomized. The Investigators were blinded during outcome assessment.

663 **Microscopy and Imaging**

664 Animals were immobilized on a 4% ultrapure agarose pad using 3-5 µL of 2-5 mM levamisole. The imaging
665 was conducted using an inverted laser scanning confocal microscope, Zeiss LSM 980, integrated with a
666 Zeiss Axio Observer 7 with Definite Focus 2. Subsequent image processing was executed via FiJi (ImageJ)
667 software.

668 **Inhibition of PHD Neurons by the HisCl method and Modified Chemoattraction Assay**

669 Inhibition of PHD neurons was achieved through the histamine-gated chloride channel method, as
670 outlined in the study [122], with slight alterations. Nematode Growth Medium containing histamine (NGM-
671 HA) was prepared by incorporating histamine dihydrochloride from Sigma Aldrich (1 M stock solution) into
672 NGM agar at approximately 65 °C just prior to pouring the plate. Control plates without histamine were
673 prepared simultaneously from the same batch of NGM. Plates supplemented with 10 mM histamine
674 remained effective for a minimum of two weeks when refrigerated at 4 °C, verified by preliminary testing
675 with a control strain possessing the *myo-2* promoter-driven HisCl effector in the cGAL-UAS system. L4-
676 stage males were selected and isolated a day in advance of the assays. Histamine treatments were
677 conducted without the presence of food to eliminate confounding factors. Histamine-induced inhibition
678 occurred within ten mins of exposure. Once removed from histamine, the animals typically require one to
679 two hours to fully recover. For PHD-specific inhibition we used the split-cGAL driver (*lin-48dP; srd-1P*)
680 crossed to 15×UAS::HisCl::SL2::GFP; animals on 10 mM histamine (NGM-HA) are referred to as 'PHD-
681 inhibited,' whereas histamine-free condition worms served as controls

682 The chemoattraction assay plates were prepared using 1.5% agar, 25 mM NaCl, 1.5 mM Tris-base, and 3.5
683 mM Tris-Cl, and conducted according to the protocol described in the literature [4], but included
684 modifications to accommodate different plate dimensions, adjustments in the spatial distance between
685 the stimulus source and the starting point of the animals, and alterations in the sex pheromone
686 concentration, as depicted in the associated figures (see Figure 1 and S1).

687 Stimulus droplets are placed on the lid of the plate, and the location of the worms is recorded every 5
688 mins up to 30 mins post-stimulation to assess their response to the introduced stimulus. In our research,
689 we utilized two sizes of plates for the assays, with effective worm-moving surfaces measuring 5.5cm and
690 8.4cm in diameter. For simplicity and clarity in labeling, these were referred to as 6-cm and 8-cm plates,
691 respectively. In our study, we employed two types of 2D chemoattraction assays distinguished by the setup
692 and calculation of the Chemoattraction Index (C.I.). For Type 1 assays, constrained by the smaller plate size,
693 a control buffer spot was not included. Here, the C.I. was derived from the ratio of worms that reached
694 the test spot to the total number of worms introduced. Conversely, in Type 2 assays, the C.I. was
695 determined by subtracting the number of worms that reached the control spot from those that arrived at
696 the test spot, divided by the total number of worms. In each chemoattraction assay, we placed 20 worms
697 at a designated starting point. To ensure the reliability and robustness of our data, we repeated each assay
698 20 times across three distinct days.

699 **Chemoattraction Assay**

Male chemotaxis was quantified using a chemoattraction assay as previously described (Wan et al., 2024). Briefly, 2 µL of pheromone extract or M9 buffer (control) was applied to designated spots on the assay plate, each supplemented with 1 M sodium azide to immobilize responding males. M9 buffer (3 g $KH_2PO_4$, 6 g $Na_2HPO_4$, 5 g NaCl, 1 mL 1 M $MgSO_4$, water to 1 L; autoclave). 20 one-day-old adult males were placed at the origin point, and chemoattraction index (C.I.) were calculated after 30 minutes using the formula: C.I. = (E − C) / (E + C + N), where E, C, and N represent the number of worms at the experimental, control, or neither spot, respectively. PHD-inhibited worms prepared via the "Inhibition of PHD Neurons by HisCl Method" .

3D chemoattraction assay employing 0.3g of gellan gum in 100ml chemoattraction assay buffer to create a navigable gel environment. This composition ensures that worms can navigate through the gel freely, without becoming immobilized by water or causing structural damage to the gel through movement. The gellan gum solution is adjusted to match the salt concentration of the chemoattraction assay plates utilized in this research.

For plate preparation, 22 ml of the gellan gum solution is poured into a 6-cm plate immediately after the gellan gum is dissolved by heating in a microwave. The solution is allowed to cool to room temperature before introducing the worms. To embed the worms within the gel, 0.5ml of the gellan gum gel is removed from the center of the plate by pipetting. Then, 20 worms are picked by worm picker and placed. This cavity is then refilled with 0.7 ml of gellan gum gel, ensuring the worms are fully embedded within the gel. Unlike traditional chemoattraction assays, the stimulus is applied directly onto the surface of the gel rather than on the lid of the plate (see Figure 2B). This approach ensures that the pheromone remains accessible to the worms and provides a localized and consistent gradient for them to follow. In this endpoint assay, trajectories are not recorded; instead, the number of worms reaching the target spot is documented every 5 minutes for up to 30 minutes post-stimulation to evaluate their responses to the introduced stimulus. This scoring method focuses on the culmination of navigational behavior, capturing the effectiveness of the worms' ability to detect and respond to the pheromone gradient over time. To ensure the reliability and robustness of our data, we repeated each assay 20 times across three distinct days. PHD-inhibited worms were prepared via the "Inhibition of PHD Neurons by HisCl Method". We remark that this C.I. quantification is not a projection onto the 2D plane, since worms at the target will stay still afterwards but those not reaching the target will move in all directions. For example, a worm at the same (x,y) coordinate as the pheromone location but vertically below the stimulus droplet (so the z coordinate is different from the droplet) will continue to move around and will not be counted when computing the C.I. To control for vertical bias, the control solution and pheromone are placed on the same z-plane, preventing preference for movement toward the surface or bottom. Therefore, the C.I. reliably identifies worms at the target location in 3D space.

We prepared plates containing 0.3% (w/v) gellan gum in M9 buffer to generate a soft hydrogel substrate in which worms could enter and locomote within the gel volume, rather than being confined to surface crawling. Importantly, this ‘penetrable’ behavior is not an intrinsic property of gellan gum, but depends strongly on gel concentration and the resulting mechanical properties. Higher gellan gum concentrations commonly used to cast firm gels (e.g., ~2–3% w/v) produce substantially stiffer matrices and are not expected to permit volumetric penetration. Accordingly, our statement refers specifically to the 0.3% (w/v) gellan-in-M9 plates used here, which we selected as the lowest concentration that maintained plate integrity while supporting robust 3D locomotion [123]. Gellan/Gelrite has been adopted for chemotaxis arenas in high-throughput screening and behavioral assays [124,125]. Penetrable gels and 3D habitats are known to elicit burrowing and other naturalistic behaviors [126-128].

**Optogenetics Perturbation Speed Analysis**

745 The optogenetics perturbation assay was conducted using Chrimson, a red-shifted channelrhodopsin,
746 following protocols outlined by the literature [82,129,130], with slight modifications. All-trans-retinal (Sigma-
747 Aldrich) was incorporated at a concentration of 500 µM into 6-cm diameter plates containing 20mL of
748 chemoattraction assay solution. One-day-old adult animals were placed on these plates and subjected to
749 a red LED stimulus using a WormLab Tracking system (MBF Biosciences). Prior to stimulation, allow 5
750 worms a 5-minute acclimation period on the assay plate. Exclusion criteria: (1) any worm that physically
751 contacted another worm during the assay; (2) any worm that reached the plate edge. Across 150 imaged
752 worms per sex, ~120 trajectories passed quality control and were analyzed. The LED stimulus was
753 administered in a pattern of 5 seconds baseline record before stimulation, and 10-60 seconds on, followed
754 by 7.5-30 seconds off, at 100% intensity across 6-8 cycles. Implement a 30-second inter-stimulus interval
755 for PHD activation. This provides sufficient time for the worm to return to a stable forward movement
756 state. Worm tracking was conducted using the same WormLab system.

757 **Dissecting Micro-behaviors Under Optogenetic Perturbation**

758 Experiments used 8-cm NGM agar plates seeded with a thin OP50 layer to prevent starvation-induced
759 behaviors. Males were transferred from ATR+ and ATR-culture plates to an assay plate. The plate was
760 mounted on a motorized stage controlled by a joystick. Individual males were tracked and recorded with
761 a 10x 0.3NA Nikon Plan Fluor objective at 10Hz. Illumination was provided by dim, red-filtered light using
762 a HOYA 52 mm R(25A) filter to minimize disturbance to the worms. For the stimulation, we used a Sola
763 Light Engine (lumencor) light source and a 607/36 nm BrightLine excitation filter. The microscope's field
764 diaphragm was adjusted such that only a small area was illuminated when the excitation light was on. We
765 used the SOLA-SE2 software to control the light source. Prior to stimulation, allow a single worm for a 5-
766 minute acclimation period on the assay plate. The male was tracked manually using the motorized stage
767 and the following stimulation regime was applied: 30 seconds without light, followed by twenty 2-second
768 tail pulses (2-second intervals), another 30-second dark period, then 30 seconds of head stimulation, and
769 a final 30-second interval without light.

770 After postprocessing, we divided the recording into 2-second segments. For each 2-second segment, we
771 tabulated the behavioral motif displayed by the male or the first behavioral transition that occurred during
772 that segment. The following behavioral motifs and transitions were included: forward, backward,
773 transition from forward to backward, transition from backward to forward movement, high-frequency
774 direction transitions (marked by frequent direction changes within the 2-second window), and self-
775 exploration (where the worm attempts to probe its own body). This analysis provides a detailed account
776 of the nuanced responses of male *C. elegans* to optogenetic perturbation, offering insights into the micro-
777 behavioral dynamics elicited by targeted neural stimulation.

778 Our analysis employs two analyses: The four-motif analysis (Figure S6) focuses on core locomotion states
779 (forward, backward) and transitions (forward to backward, backward to forward). In the four-motif
780 analysis, transitions (e.g., forward-to-backward, backward-to-forward) were classified based on the initial
781 and final directions observed within the 2-second window. For example, a segment with rapid oscillations
782 between forward and backward movement was categorized as "forward-to-backward" if the net
783 directionality shifted from forward to backward, or vice versa.

784 The six-motif analysis (Figure 4) expands categorization to include self-exploratory and high-frequency
785 direction transitions, which capture other behaviors that cannot be easily classified as the "four-motif".
786 The high-frequency direction transitions, motif specifically identifies intervals with more than 2 direction
787 changes within a 2-second window, representing a distinct exploratory strategy that cannot be
788 unambiguously assigned to single transitions (forward to backward or backward to forward).

789 **Sex Pheromone-Induced Pan-neuronal Calcium Imaging**

790 For sex pheromone extraction, we processed 100 virgin *fog-2* female *C. elegans* by isolating them in 1 ml
791 of NGM buffer within an Eppendorf tube, following a protocol slightly modified from the previous study [4].
792 These females were washed five times to clear bacterial contamination, then incubated in 100 µl of NGM
793 or M9 buffer for 6 hours. A parallel extraction process utilized for *C. remanei* involved similar steps but
794 with only 5 females.

795 In Figure 1C, to evaluate PHD activation upon exposure to the volatile pheromone, we performed calcium
796 imaging with a custom-built spinning disk confocal microscope setup [49,74]. Utilizing the ZM9627 strain,
797 which marks all neuronal nuclei with GCaMP6s and mNeptune [74] and incorporates *him-5(e1490)* mutation
798 to enrich for males. We also crossed ZM9627 with the CB5414 *srd-1(eh1)* line. Preparation for imaging
799 involved isolating L4 males 15-20 hours in advance, placing them on 10% agar NGM buffer slides.

800 The Thin Layer Micro-Diffusion (TLMD) method was adapted from Wan et al. [4] (see Figure S9A). Neuronal
801 excitation was detected by measuring changes in fluorescence intensity using a disposable worm-
802 mounting and a chemical-loading device called the thin-layer micro-diffusion (TLMD) unit. The TLMD unit
803 consisted of a 4% agarose pad (0.2 mm thick, 1.3 mm radius) sandwiched between two autoclave tapes.
804 Before mounting, well-fed transgenic worms were transferred to an empty worm plate for 5 minutes to
805 remove residual bacteria. A 0.2 µL of 1 mM levamisole was then applied to the agarose pad to partially
806 immobilize the worms, which were positioned uniformly with their heads facing outward. A clean 22 × 40
807 mm coverslip was gently placed over the TLMD unit. At the 30-second time point, 8 µL of the test chemical
808 solution was loaded. Due to capillary action, the solution rapidly filled the space between the slide and
809 coverslip. Chemical diffusion began immediately (within milliseconds) as the micro-gel pad became
810 surrounded by the loaded solution. Approximately 5 ul of 0.2 um latex beads (Polysciences, Inc.) were
811 added to aid immobilization.

812 Imaging was conducted with a 40x 0.95 NA objective, achieving 200 Hz to record 10 volumes per second,
813 with each comprising 20 optical slices. Pheromone or control buffer introduction occurred 30 seconds
814 after initiating imaging, continuing for an additional 3.5-9.5 mins. Subsequent processing and registration
815 allowed for tracking PHD neuron nuclei using semi-automated methods in MAMUT [117]. Intensities from
816 GCaMP and mNeptune channels were extracted for analysis within defined ROIs, calculating neuronal
817 activity ratios and smoothing data with Savitzky-Golay filters. The activity was quantified by normalizing
818 GCaMP fluorescence against mNeptune. We used the ratio R=F(GCaMP)/F(mNeptune), after applying
819 Savitzky-Golay filtering to each channel (polynomial order 1 and length 13) Relative intensity values ($\Delta R/R_o$)
820 were calculated as $(R-R_0)/R_0$, where raw fluorescence intensity ratio (R) was extracted from the region of
821 interest (ROI) of the target neuron in the calcium imaging data, and $R_o$ is the baseline fluorescence, defined
822 as the mean fluorescence during the quiescent period. Analyses were performed using custom code.

823 In Figure 5, our study employed the same custom-built spinning disk confocal microscope setup mentioned
824 above and a sparse labeling markers pan-neuronal calcium imaging strain, ADS1046, which features a dual
825 expression of the calcium indicator GCaMP6s and the red fluorescent protein mNeptune in all neuronal
826 nuclei, alongside the *lite-1(ce314)* mutation to eliminate undesired light-induced neural activity. This strain
827 also has sparse labeling markers (*Pift-20*:BFP, P*eat-4*:cyOFP1, P*unc-17*:mScarlet, P*acr-5*:BFP) for neuron
828 identification. Intracellular calcium dynamics were quantified by tracking the calcium indicator GCaMP6s
829 signals, which enhances green fluorescence intensity within cells. Concurrently, mNeptune signals were
830 captured to serve as a reference. The intensity ratio of GCaMP to mNeptune (GFP/RFP) at each time point
831 was plotted. To aid neuron identification, after the recording session, we acquired additional volumes using
832 the following combination of excitation lasers and emission filters: 30% 640 nm 617/73 nm (200 Hz), 40%

561 nm 578 nm (200 Hz), 35% 488 nm 578 nm (200 Hz), 15% 488 nm (200 Hz), 95% 405 nm 440 or 450 nm (50Hz).

We fit the activity of AVA neurons by a linear combination of AWA and PHD neurons by minimizing the least-squared error (Figure 5F).

**Neuron Tracking**

Each neuron was automatically tracked through all 3D volumes with targettrack. We first applied a strong low pass filter to blur the whole image and thresholded it to find the general location of the head or tail. After centering each volume by the region found above, we cropped a rectangular ROI that covered the whole region for 99% of the recording. Then, we manually identified AWA, ASI, AVA, AVE, PHD neurons in each recording and annotated an average of 5 frames per recording. We used targettrack [119] to automatically segment and track each neuron in every volume. We trained the 3DCN of targettrack for 10K gradient steps with a batch size of 3. The quality of the tracking was manually verified after tracking.

The xyz coordinates were used to extract pixel intensities around neuronal nuclei. These changes were then standardized against the baseline pre-stimulation background, resulting in the relative intensity values (ΔR/R0) being displayed. Data representation is in the form of mean ± standard error of the mean (s.e.m.), processed using Graphpad Prism 6 and Microsoft Excel for comprehensive analysis. Custom Matlab code was utilized for graphing, with the $\Delta R/R_0$ average depicted by a black line and the s.e.m. by a gray-shaded envelope. The duration of stimulation is visually encoded on the plots with a pink color bar.

**Pan-neuronal calcium imaging with optogenetic activation**

This experiment used the same sparse labeling makers, pan-neuronal calcium imaging strain mentioned previously. For optogenetic activation we expressed Chrimson using an *srd-1P*::Gal4(sk)::VP64 driver crossed to 15×UAS::Chrimson effector in the pan-neuronal imaging background; animals were reared ± ATR. During imaging we delivered defined light stimuli; only ATR+ animals under light showed Chrimson-dependent responses. For the experiments, males were prepared on 10% agar NGM buffer slides. Using a spinning disc confocal setup, we navigated the challenge of simultaneous neuronal imaging and optogenetic stimulation of Chrimson, which responds to both 488 nm and 578 nm light, by implementing a strategy to exploit the GCaMP signal delay post-stimulation, as outlined in Lu et al. (2022) [131]. This involved interlacing five 10-second imaging/stimulation intervals with 50-second breaks, applying 12% and 35% intensities for the 488 nm and 561 nm lasers, respectively, while acknowledging potential mechanical stimulation from objective movement as a confounding variable. During each 5-second imaging/activation period the piezo-controlled objective was moving, whereas it was not moving between these periods. We therefore cannot rule out mechanical stimulation that coincided with light stimulation as a confounding factor. To aid neuron identification, after the recording session, we acquired additional volumes using the following combination of excitation lasers and emission filters: 30% 640 nm 617/73 nm (200 Hz), 40% 561 nm 578 nm (200 Hz), 35% 488 nm 578 nm (200 Hz), 15% 488 nm (200 Hz), 95% 405 nm 440 or 450 nm (50Hz).

The same pre-processing and neuron activity tracking via Targettrack was performed as outlined in "Neuron Tracking". For each neuron, we created 3 ground truth points, 100 volumes apart. Activities of PHD neurons in ATR+ and ATR- males were extracted and averaged. We calculated the correlation between the mean PHD activity in ATR+ males and activity traces of other neurons in both ATR+ and ATR- males. A subset of 12 neurons was identified across all males and we used Generalized Procrustes analysis [132] and thin plate splines [133] to register all male tail neurons to a common coordinate space. These landmark neurons were: PHDR, PHDL, PLMR, PCAR, PCAL, HOA, PVY, PDC, PVX, VD12, VA10, and VA11. A visual inspection identified two regions that contain neurons highly correlated with PHD (correlation

877 cutoff >0.55). Here we refer to these regions as ROI1 and ROI2 (see Figure 5 and S6). AWA, ASI, AVA and
878 AVE are identified based on sparse labeling makers, positioning and cell body size. The relative intensity
879 values (ΔR/R0) are plotted following the methodology outlined in "Sex Pheromone-Induced Pan-neuronal
880 Calcium Imaging in *C. elegans*" with minor modifications. We normalized the ΔR/R0 values for each neuron
881 in the ATR+ and ATR- groups to a range of 0 to 1. The dashed line indicated the starting point of each light
882 stimulation.

883 **Microfluidic chip design and manufacturing**

884 The design of our microfluidic devices is accomplished using SolidWorks software, tailored to the specific
885 requirements of our experiments. The fabrication process utilizes both photolithography and
886 polydimethylsiloxane (PDMS) soft lithography, as detailed in the literature [51,134]. Initially, 3-inch silicon
887 wafers were prepared by coating with a layer of SU-8 photoresist. This layer was subsequently patterned
888 through photolithography, transforming the wafer into a mold for PDMS casting. For constructs intended
889 for male worm imaging, the SU-8 2015 photoresist was spun at 1450 rpm to achieve a thickness of 24-25
890 µm. Following PDMS casting, the microfluidic devices were bonded to glass coverslips using a plasma
891 cleaner, employing settings of 50mW power for 30 seconds to ensure a robust bond. This fabrication
892 procedure is designed to produce precise microfluidic devices, enabling the simultaneous and individual
893 delivery of stimulus to the head and tail regions of *C. elegans* males, while also facilitating concurrent
894 calcium imaging. This chip allows for accurate delivery of stimulus to both the head and tail regions
895 separately, with 4 inlets dedicated to each region and an additional outlet for waste. An optimized worm
896 trapper adaptor from a previous study [135], secures males for imaging while ensuring both ends remain
897 exposed to the stimulus channels. Designed stoppers within the tail inlet channels prevent the worms
898 from escaping during injection, without disrupting fluid flow. This approach allows for the detailed study
899 of neural responses to localized stimuli in a controlled environment.

900 **Sex pheromone preparation for microfluidics chip-based experiments**

901 To obtain large quantities of crude sex pheromone for microfluidics chip-based experiments, we modified
902 the standard extraction protocol to avoid the time-consuming isolation of L4 stage *fog-2* females. We used
903 5-day-old *daf-22* mutant *C. elegans* hermaphrodites, which lack ascaroside synthesis, to ensure the
904 absence of confounding neuronal responses from this water-soluble sex pheromone stimulus. Bleach-
905 synchronized *daf-22* mutant worms were washed five times with M9 buffer. L1 stage arrest was induced
906 by rotating worms in M9 buffer for 12 hours before seeding on culture plates (8-cm NGM with OP50,
907 approximately 500 L1 worms/plate). Adult worms were collected after three days (at the onset of egg-
908 laying). Adults were washed from culture plates with M9 buffer and separated from eggs using the
909 precipitation method (repeated 5-7 times until eggs were absent). Separated adults were transferred to
910 new OP50-seeded plates, and this washing process was repeated for 6 days to exhaust self-sperm. Sex
911 pheromone extraction was performed as described in "sex pheromone-induced pan-neuronal calcium
912 imaging" with the following modification: instead of 100 worms/mL, we used 50 µl of packed worm
913 volume per 1 mL of M9 buffer (see Figure S10 A-C). Three batches of extracted pheromone were tested
914 for quality using a chemoattraction assay and combined to create a 100 ml homogenous stimulus for
915 microfluidics chip-based experiments.

916 **Microfluidics chip-based experiment calcium imaging and data analysis**

917 Young adult *C. elegans* males (PS10181) were loaded into a custom microfluidic chip that allows selective
918 exposure of head and tail to odor solutions of choice. Solution administration was directed by an array of
919 8 memory-shape alloy valves (Takasago Fluidics Inc., Japan) individually addressed by an ESP32
920 microcontroller. Imaging was performed using a Leica DM6000 B microscope equipped with a X-Cite XLED1

Multi-Triggering LED illumination system (Excelitas Technologies) and iXon EMCCD detectors (Oxford Instruments Andor). Image acquisition and microfluidic stimulation administration were controlled and synchronized by a custom Python graphic interface using the Pycro-Manager interface for the Micro-Manager microscope control software [136]. Time-lapse image segmentation was performed using the pixel classification function of the Ilastik software and intensity values of GCaMP and RFP were extracted using a custom Jupyter notebook. The calcium imaging traces were calculated as the ratio of GCaMP6s/RFP fluorescence to correct for out-of-plane imaging artifacts. Because of the high background activity of the AVA neuron, baseline values for the calculation of the $\Delta R/R_0$ metric were estimated using the peakutils Python package. The relative intensity values ($\Delta R/R_0$) are plotted following the methodology outlined in "Sex Pheromone-Induced Pan-neuronal calcium imaging in *C. elegans*," with minor modifications. To quantify the effect of suppression/excitation on AVA neuron, we performed area-under-curve (AUC) analysis. We first compute the baseline AVA activity by averaging over 3 mins before stimulation given at the most dilute concentration and subtract this baseline value from all signals. Then we integrate the area under curve for each worm data for 2 mins after the stimulation. For suppression, we only account for time intervals when the signal is lower than the baseline value; for excitation, we only account for time intervals when the signal is higher than the baseline value so that to naturally terminate the integration of area when the signal disappears. In Figure 6D, we compute the linear combination of AVA neuron activities with only head or tail stimulation ($AVA_{head}$+$AVA_{tail}$) and compare that with the AVA neuron activity with simultaneous head and tail stimulation ($AVA_{dual}$).

**Concentration field simulation**

The concentration evolution inside the petri dishes was simulated using the Finite Element method. The simulated plates consist of a top layer of 4mm thick air and a bottom layer of 9mm thick agar. The diffusion coefficient of the sex pheromone was estimated $1.6\ mm^2/s$ in the air and $10^{-3}\ mm^2/s$ in the agar. The initial condition was set as concentration at the surface of the droplet $c_0 = 0.01\ mol/m^3$ while $c_0 = 0$ elsewhere. No-flux boundary condition was applied to the walls of the plate. For the dynamical simulations of worm searching, we take the 2D cross-section of the concentration field at z=-0.5 mm inside the agar (the air-agar interface is at z=0).

**Navigation simulation**

The navigation processes were simulated using an in-house extension of the HOOMD-Blue package. Mathematically, worm locomotion dynamics are described by the following equations:

$$d\boldsymbol{r} = \boldsymbol{Uqdt}, \boldsymbol{q} = (\cos\boldsymbol{\theta}, \sin\boldsymbol{\theta}), \boldsymbol{d\theta} = \sqrt{\boldsymbol{2D_R}}\boldsymbol{dW_S} + \boldsymbol{\gamma dW_T}. \quad (3)$$

Here, $\boldsymbol{r}$ is the position of the worm, U the speed magnitude, **q** the orientation direction, $D_R$ the rotary diffusivity of the orientation angle $\theta$. $dW_S$ and $dW_T$ denote the standard Brownian motion on a circle $-\pi < \theta < \pi$ and a Poisson jump process respectively. $\boldsymbol{\gamma}$ is the intensity of the jump process, i.e., the tumbling rate. It has been observed [137] that during tumbles (large angle turns), the turning angle distribution displays a peak near π. Empirically, we represent the turning angle distribution as a mixture of uniform distribution and a wrapped Gaussian distribution:

$$T(\theta, \theta') = \alpha T_0 + (1-\alpha)T_1. \quad (4)$$

Here the turning kernel $T(\theta, \theta')$ is the probability of turning from $\theta'$ direction to $\theta$ direction. $T_0 = 1/(2\pi)$ is the uniform distribution and $T_1 = e^{-\frac{(\theta-\pi)^2}{2\sigma^2}}$ is a wrapped Gaussian distribution.

We adopt the following functional forms to reflect the above observed sensory neuron dynamics:

$$f_H = \frac{\dot{C}}{\dot{C_0}}\frac{1+tanh(log(C/C_0))}{2},$$

$$f_T = \begin{cases} e^{-(\log(C/C_0))^2} \text{if } C \le C_0 \\ 1-(\log(C/C_0))^2 \text{if } C > C_0 \end{cases} \quad (5)$$

In the simulations, we fix $D_R = 0.02, \eta = 1, k_1 = 1/60, k_2^{H,T} = 1$.

**Data availability**

The data generated in this study have been deposited at the GitHub repository (pheromone-traj-analysis) https://github.com/edmondztt/pheromone-traj-analysis[138]. Calcium imaging and behavioral datasets supporting Figs. 1, 4, 7 and Supplementary Figs. S1, S3, S5, S11 are available from the CaltechDATA repository https://doi.org/10.22002/dp6gb-ky687[139]. Source data are provided with this paper.

**Code availability**

The code used for data processing and analysis in this study is publicly available at https://github.com/edmondztt/pheromone-traj-analysis[138].

**References:**


1 Simon, J. M. & Sternberg, P. W. Evidence of a mate-finding cue in the hermaphrodite nematode *Caenorhabditis elegans*. *Proceedings of the National Academy of Sciences* **99**, 1598-1603 (2002).

2 Lipton, J., Kleemann, G., Ghosh, R., Lints, R. & Emmons, S. W. Mate searching in *Caenorhabditis elegans*: a genetic model for sex drive in a simple invertebrate. *The Journal of neuroscience : the official journal of the Society for Neuroscience* **24**, 7427-7434, doi:10.1523/JNEUROSCI.1746-04.2004 [doi] (2004).

3 Leighton, D. H., Choe, A., Wu, S. Y. & Sternberg, P. W. Communication between oocytes and somatic cells regulates volatile pheromone production in *Caenorhabditis elegans*. *Proc Natl Acad Sci U S A* **111**, 17905-17910, doi:10.1073/pnas.1420439111 (2014).

4 Wan, X. *et al.* SRD-1 in AWA neurons is the receptor for female volatile sex pheromones in *C. elegans* males. *EMBO Rep* **20**, doi:10.15252/embr.201846288 (2019).

5 Chasnov, J. R., So, W. K., Chan, C. M. & Chow, K. L. The species, sex, and stage specificity of a *Caenorhabditis* sex pheromone. *Proc Natl Acad Sci U S A* **104**, 6730-6735, doi:10.1073/pnas.0608050104 (2007).

6 Lockery, S. R. The computational worm: spatial orientation and its neuronal basis in *C. elegans*. *Current opinion in neurobiology* **21**, 782-790 (2011).

7 Schone, H. *Spatial orientation: The spatial control of behavior in animals and man*. Vol. 588 (Princeton University Press, 2014).

8 Grasso, F. W. & Basil, J. A. How lobsters, crayfishes, and crabs locate sources of odor: current perspectives and future directions. *Current opinion in neurobiology* **12**, 721-727 (2002).

9 Gomez-Diaz, C. & Benton, R. The joy of sex pheromones. *EMBO reports* **14**, 874-883, doi:10.1038/embor.2013.140 [doi] (2013).

10 Moncho-Bogani, J., Lanuza, E., Lorente, M. J. & Martinez-Garcia, F. Attraction to male pheromones and sexual behaviour show different regulatory mechanisms in female mice. *Physiol Behav* **81**, 427-434, doi:10.1016/j.physbeh.2004.01.014 (2004).

11 Moncho-Bogani, J., Martinez-Garcia, F., Novejarque, A. & Lanuza, E. Attraction to sexual pheromones and associated odorants in female mice involves activation of the reward system and

1002 basolateral amygdala. *Eur J Neurosci* **21**, 2186-2198, doi:10.1111/j.1460-9568.2005.04036.x
1003 (2005).

1004 12 Kurtovic, A., Widmer, A. & Dickson, B. J. A single class of olfactory neurons mediates behavioural
1005 responses to a Drosophila sex pheromone. *Nature* **446**, 542-546 (2007).

1006 13 Stockinger, P., Kvitsiani, D., Rotkopf, S., Tirián, L. & Dickson, B. J. Neural circuitry that governs
1007 Drosophila male courtship behavior. *Cell* **121**, 795-807 (2005).

1008 14 Datta, S. R. *et al.* The Drosophila pheromone cVA activates a sexually dimorphic neural circuit.
1009 *Nature* **452**, 473-477 (2008).

1010 15 Miyamoto, T. & Amrein, H. Suppression of male courtship by a Drosophila pheromone receptor.
1011 *Nature neuroscience* **11**, 874-876 (2008).

1012 16 Ruta, V. *et al.* A dimorphic pheromone circuit in Drosophila from sensory input to descending
1013 output. *Nature* **468**, 686-690 (2010).

1014 17 Hofman, M. A. & Swaab, D. F. The sexually dimorphic nucleus of the preoptic area in the human
1015 brain: a comparative morphometric study. *Journal of anatomy* **164**, 55 (1989).

1016 18 Wei, D., Talwar, V. & Lin, D. Neural circuits of social behaviors: Innate yet flexible. *Neuron* **109**,
1017 1600-1620 (2021).

1018 19 Auer, T. O. & Benton, R. Sexual circuitry in Drosophila. *Current opinion in neurobiology* **38**, 18-26
1019 (2016).

1020 20 Yang, C. F. & Shah, N. M. Representing sex in the brain, one module at a time. *Neuron* **82**, 261-278
1021 (2014).

1022 21 De Vries, G. J. & Simerly, R. B. in *Hormones, brain and behavior* 137-XXIX (Elsevier, 2002).

1023 22 Cachero, S., Ostrovsky, A. D., Jai, Y. Y., Dickson, B. J. & Jefferis, G. S. Sexual dimorphism in the fly
1024 brain. *Current biology* **20**, 1589-1601 (2010).

1025 23 Peckol, E. L., Troemel, E. R. & Bargmann, C. I. Sensory experience and sensory activity regulate
1026 chemosensory receptor gene expression in *Caenorhabditis elegans*. *Proceedings of the National*
1027 *Academy of Sciences of the United States of America* **98**, 11032-11038,
1028 doi:10.1073/pnas.191352498 [doi] (2001).

1029 24 Ludewig, A. H. *et al.* Pheromone sensing regulates *Caenorhabditis elegans* lifespan and stress
1030 resistance via the deacetylase SIR-2.1. *Proc Natl Acad Sci U S A* **110**, 5522-5527,
1031 doi:10.1073/pnas.1214467110 (2013).

1032 25 Golden, J. W. & Riddle, D. L. A pheromone influences larval development in the nematode
1033 *Caenorhabditis elegans*. *Science* **218**, 578-580, doi:10.1126/science.6896933 (1982).

1034 26 Butcher, R. A., Fujita, M., Schroeder, F. C. & Clardy, J. Small-molecule pheromones that control
1035 dauer development in *Caenorhabditis elegans*. *Nature chemical biology* **3**, 420-422 (2007).

1036 27 Jeong, P. Y. *et al.* Chemical structure and biological activity of the *Caenorhabditis elegans* dauer-
1037 inducing pheromone. *Nature* **433**, 541-545, doi:10.1038/nature03201 (2005).

1038 28 Butcher, R. A., Ragains, J. R., Kim, E. & Clardy, J. A potent dauer pheromone component in
1039 *Caenorhabditis elegans* that acts synergistically with other components. *Proc Natl Acad Sci U S A*
1040 **105**, 14288-14292, doi:10.1073/pnas.0806676105 (2008).

1041 29 Aprison, E. Z. & Ruvinsky, I. Counteracting Ascarosides Act through Distinct Neurons to Determine
1042 the Sexual Identity of *C. elegans* Pheromones. *Curr Biol* **27**, 2589-2599 e2583,
1043 doi:10.1016/j.cub.2017.07.034 (2017).

1044 30 Aprison, E. Z. & Ruvinsky, I. Sex Pheromones of *C. elegans* Males Prime the Female Reproductive
1045 System and Ameliorate the Effects of Heat Stress. *PLoS Genet* **11**, e1005729,
1046 doi:10.1371/journal.pgen.1005729 (2015).

1047 31 Kaplan, F. *et al.* Ascaroside expression in *Caenorhabditis elegans* is strongly dependent on diet and
1048 developmental stage. *PLoS One* **6**, e17804, doi:10.1371/journal.pone.0017804 (2011).

1049 32 Srinivasan, J. *et al.* A modular library of small molecule signals regulates social behaviors in
1050 *Caenorhabditis elegans*. *PLoS biology* **10**, e1001237 (2012).

1051 33 Srinivasan, J. *et al.* A blend of small molecules regulates both mating and development in
1052 *Caenorhabditis elegans*. *Nature* **454**, 1115-1118 (2008).

1053 34 Ludewig, A. H. & Schroeder, F. C. Ascaroside signaling in *C. elegans*. *WormBook*, 1-22,
1054 doi:10.1895/wormbook.1.155.1 (2013).

1055 35 Choe, A. *et al.* Ascaroside signaling is widely conserved among nematodes. *Curr Biol* **22**, 772-780,
1056 doi:10.1016/j.cub.2012.03.024 (2012).

1057 36 von Reuss, S. H. *et al.* Comparative metabolomics reveals biogenesis of ascarosides, a modular
1058 library of small-molecule signals in *C. elegans*. *J Am Chem Soc* **134**, 1817-1824,
1059 doi:10.1021/ja210202y (2012).

1060 37 Choe, A. *et al.* Sex-specific mating pheromones in the nematode Panagrellus redivivus. *Proc Natl*
1061 *Acad Sci U S A* **109**, 20949-20954, doi:10.1073/pnas.1218302109 (2012).

1062 38 Hsueh, Y. P., Mahanti, P., Schroeder, F. C. & Sternberg, P. W. Nematode-trapping fungi eavesdrop
1063 on nematode pheromones. *Curr Biol* **23**, 83-86, doi:10.1016/j.cub.2012.11.035 (2013).

1064 39 Pungaliya, C. *et al.* A shortcut to identifying small molecule signals that regulate behavior and
1065 development in *Caenorhabditis elegans*. *Proc Natl Acad Sci U S A* **106**, 7708-7713,
1066 doi:10.1073/pnas.0811918106 (2009).

1067 40 Izrayelit, Y. *et al.* Targeted metabolomics reveals a male pheromone and sex-specific ascaroside
1068 biosynthesis in *Caenorhabditis elegans*. *ACS chemical biology* **7**, 1321-1325 (2012).

1069 41 Fagan, K. A. *et al.* A Single-Neuron Chemosensory Switch Determines the Valence of a Sexually
1070 Dimorphic Sensory Behavior. *Curr Biol* **28**, 902-914 e905, doi:10.1016/j.cub.2018.02.029 (2018).

1071 42 Chasnov, J. R., So, W. K., Chan, C. M. & Chow, K. L. The species, sex, and stage specificity of a
1072 *Caenorhabditis* sex pheromone. *Proceedings of the National Academy of Sciences of the United*
1073 *States of America* **104**, 6730-6735, doi:0608050104 [pii] (2007).

1074 43 Kato, S., Xu, Y., Cho, C. E., Abbott, L. & Bargmann, C. I. Temporal responses of *C. elegans*
1075 chemosensory neurons are preserved in behavioral dynamics. *Neuron* **81**, 616-628 (2014).

44 Luo, L. *et al.* Dynamic encoding of perception, memory, and movement in a *C. elegans* chemotaxis circuit. *Neuron* **82**, 1115-1128 (2014).

45 Wang, L. *et al.* A gustatory neural circuit of *Caenorhabditis elegans* generates memory-dependent behaviors in Na+ chemotaxis. *Journal of Neuroscience* **37**, 2097-2111 (2017).

46 Satoh, Y. *et al.* Regulation of experience-dependent bidirectional chemotaxis by a neural circuit switch in *Caenorhabditis elegans*. *Journal of Neuroscience* **34**, 15631-15637 (2014).

47 Kunitomo, H. *et al.* Concentration memory-dependent synaptic plasticity of a taste circuit regulates salt concentration chemotaxis in *Caenorhabditis elegans*. *Nature communications* **4**, 2210 (2013).

48 Ji, N. *et al.* Corollary discharge promotes a sustained motor state in a neural circuit for navigation. *Elife* **10**, e68848 (2021).

49 Venkatachalam, V. *et al.* Pan-neuronal imaging in roaming *Caenorhabditis elegans*. *Proceedings of the National Academy of Sciences* **113**, E1082-E1088 (2016).

50 Zhen, M. & Samuel, A. D. *C. elegans* locomotion: small circuits, complex functions. *Current opinion in neurobiology* **33**, 117-126 (2015).

51 Chalasani, S. H. *et al.* Dissecting a circuit for olfactory behaviour in *Caenorhabditis elegans*. *Nature* **450**, 63-70 (2007).

52 Gray, J. M., Hill, J. J. & Bargmann, C. I. A circuit for navigation in *Caenorhabditis elegans*. *Proceedings of the National Academy of Sciences* **102**, 3184-3191 (2005).

53 Larsch, J. *et al.* A circuit for gradient climbing in *C. elegans* chemotaxis. *Cell reports* **12**, 1748-1760 (2015).

54 Dobosiewicz, M., Liu, Q. & Bargmann, C. I. Reliability of an interneuron response depends on an integrated sensory state. *Elife* **8**, e50566 (2019).

55 Luo, L. *et al.* Bidirectional thermotaxis in *Caenorhabditis elegans* is mediated by distinct sensorimotor strategies driven by the AFD thermosensory neurons. *Proceedings of the National Academy of Sciences* **111**, 2776-2781 (2014).

56 Colbert, H. A. & Bargmann, C. I. Environmental signals modulate olfactory acuity, discrimination, and memory in *Caenorhabditis elegans*. *Learning & memory (Cold Spring Harbor, N.Y.)* **4**, 179-191 (1997).

57 Wen, J. Y. M. *et al.* Mutations that prevent associative learning in *C. elegans*. *Behavioral neuroscience* **111**, 354 (1997).

58 Saeki, S., Yamamoto, M. & Iino, Y. Plasticity of chemotaxis revealed by paired presentation of a chemoattractant and starvation in the nematode *Caenorhabditis elegans*. *The Journal of experimental biology* **204**, 1757-1764 (2001).

59 Nuttley, W. M., Atkinson-Leadbeater, K. P. & Van Der Kooy, D. Serotonin mediates food-odor associative learning in the nematode *Caenorhabditis*elegans. *Proceedings of the National Academy of Sciences of the United States of America* **99**, 12449-12454, doi:10.1073/pnas.192101699 [doi] (2002).

1114 60 Zhang, Y., Lu, H. & Bargmann, C. I. Pathogenic bacteria induce aversive olfactory learning in
1115 *Caenorhabditis elegans*. *Nature* **438**, 179-184 (2005).

1116 61 Vellai, T., McCulloch, D., Gems, D. & Kovács, A. L. Effects of sex and insulin/insulin-like growth
1117 factor-1 signaling on performance in an associative learning paradigm in *Caenorhabditis elegans*.
1118 *Genetics* **174**, 309-316 (2006).

1119 62 Kauffman, A. *et al. C. elegans* positive butanone learning, short-term, and long-term associative
1120 memory assays. *J Vis Exp*, doi:10.3791/2490 (2011).

1121 63 Sakai, N. *et al.* A sexually conditioned switch of chemosensory behavior in *C. elegans*. *PLoS One* **8**,
1122 e68676, doi:10.1371/journal.pone.0068676 (2013).

1123 64 Stein, G. M. & Murphy, C. T. *C. elegans* positive olfactory associative memory is a molecularly
1124 conserved behavioral paradigm. *Neurobiol Learn Mem* **115**, 86-94, doi:10.1016/j.nlm.2014.07.011
1125 (2014).

1126 65 Hong, M. *et al.* Early Pheromone Experience Modifies a Synaptic Activity to Influence Adult
1127 Pheromone Responses of *C. elegans*. *Curr Biol* **27**, 3168-3177 e3163,
1128 doi:10.1016/j.cub.2017.08.068 (2017).

1129 66 Gordus, A., Pokala, N., Levy, S., Flavell, S. W. & Bargmann, C. I. Feedback from network states
1130 generates variability in a probabilistic olfactory circuit. *Cell* **161**, 215-227 (2015).

1131 67 Hilliard, M. A., Bargmann, C. I. & Bazzicalupo, P. *C. elegans* responds to chemical repellents by
1132 integrating sensory inputs from the head and the tail. *Current Biology* **12**, 730-734 (2002).

1133 68 Gat, A. *et al.* Integration of spatially opposing cues by a single interneuron guides decision making
1134 in *C. elegans*. *bioRxiv*, 2023.2001. 2023.525194 (2023).

1135 69 Quintin, S., Aspert, T., Ye, T. & Charvin, G. Distinct mechanisms underlie H2O2 sensing in *C. elegans*
1136 head and tail. *Plos one* **17**, e0274226 (2022).

1137 70 Troemel, E. R., Chou, J. H., Dwyer, N. D., Colbert, H. A. & Bargmann, C. I. Divergent seven
1138 transmembrane receptors are candidate chemosensory receptors in *C. elegans*. *Cell* **83**, 207-218
1139 (1995).

1140 71 Yi, W., Ross, J. M. & Zarkower, D. Mab-3 is a direct tra-1 target gene regulating diverse aspects of
1141 *C. elegans* male sexual development and behavior. *Development* **127**, 4469-4480 (2000).

1142 72 Molina-García, L. *et al.* Direct glia-to-neuron transdifferentiation gives rise to a pair of male-
1143 specific neurons that ensure nimble male mating. *Elife* **9**, e48361 (2020).

1144 73 Morillo, K. S., St. Ange, J., Weng, Y., Kaletsky, R. & Murphy, C. T. Single-Nucleus Neuronal
1145 Transcriptional Profiling of Male *C. elegans* Uncovers Regulators of Sex-Specific and Sex-Shared
1146 Behaviors. *bioRxiv*, 2024.2012. 2012.628226 (2024).

1147 74 Susoy, V. *et al.* Natural sensory context drives diverse brain-wide activity during *C. elegans* mating.
1148 *Cell* **184**, 5122-5137. e5117 (2021).

1149 75 Sengupta, P., Chou, J. H. & Bargmann, C. I. odr-10 encodes a seven transmembrane domain
1150 olfactory receptor required for responses to the odorant diacetyl. *Cell* **84**, 899-909,
1151 doi:10.1016/s0092-8674(00)81068-5 (1996).

76 Bargmann, C. I. Chemosensation in *C. elegans*. *WormBook : the online review of C.elegans biology*, 1-29, doi:10.1895/wormbook.1.123.1 [doi] (2006).

77 Ferkey, D. M., Sengupta, P. & L'Etoile, N. D. Chemosensory signal transduction in *Caenorhabditis elegans*. *Genetics* **217**, iyab004 (2021).

78 Im Choi, J. *et al.* Odor-dependent temporal dynamics in Caenorhabitis elegans adaptation and aversive learning behavior. *PeerJ* **6**, e4956 (2018).

79 Bargmann, C. I., Hartwieg, E. & Horvitz, H. R. Odorant-selective genes and neurons mediate olfaction in *C. elegans*. *Cell* **74**, 515-527 (1993).

80 Tran, A. *et al. C. elegans* avoids toxin-producing Streptomyces using a seven transmembrane domain chemosensory receptor. *Elife* **6**, e23770 (2017).

81 Zhou, Y. *et al.* Potential Nematode Alarm Pheromone Induces Acute Avoidance in *Caenorhabditis elegans*. *Genetics* **206**, 1469-1478, doi:10.1534/genetics.116.197293 (2017).

82 Klapoetke, N. C. *et al.* Independent optical excitation of distinct neural populations. *Nature methods* **11**, 338-346 (2014).

83 Cook, S. J. *et al.* Whole-animal connectomes of both *Caenorhabditis elegans* sexes. *Nature* **571**, 63-71 (2019).

84 Cohen, N. & Denham, J. E. Whole animal modeling: piecing together nematode locomotion. *Current Opinion in Systems Biology* **13**, 150-160 (2019).

85 Kato, S. *et al.* Global brain dynamics embed the motor command sequence of *Caenorhabditis elegans*. *Cell* **163**, 656-669 (2015).

86 Meng, J. *et al.* A tonically active master neuron modulates mutually exclusive motor states at two timescales. (2023).

87 Choi, M.-K., Liu, H., Wu, T., Yang, W. & Zhang, Y. NMDAR-mediated modulation of gap junction circuit regulates olfactory learning in *C. elegans*. *Nature Communications* **11**, 3467 (2020).

88 Marvin, J. S. *et al.* An optimized fluorescent probe for visualizing glutamate neurotransmission. *Nature methods* **10**, 162-170 (2013).

89 Albrecht, D. R. & Bargmann, C. I. High-content behavioral analysis of *Caenorhabditis elegans* in precise spatiotemporal chemical environments. *Nature methods* **8**, 599-605 (2011).

90 Cheung, B. H., Cohen, M., Rogers, C., Albayram, O. & De Bono, M. Experience-dependent modulation of *C. elegans* behavior by ambient oxygen. *Current Biology* **15**, 905-917 (2005).

91 Bretscher, A. J. *et al.* Temperature, oxygen, and salt-sensing neurons in *C. elegans* are carbon dioxide sensors that control avoidance behavior. *Neuron* **69**, 1099-1113, doi:10.1016/j.neuron.2011.02.023 (2011).

92 Ryu, W. S. & Samuel, A. D. Thermotaxis in *Caenorhabditis elegans* analyzed by measuring responses to defined thermal stimuli. *Journal of Neuroscience* **22**, 5727-5733 (2002).

93 Gabel, C. V. *et al.* Neural circuits mediate electrosensory behavior in *Caenorhabditis elegans*. *Journal of Neuroscience* **27**, 7586-7596 (2007).

1189 94 Sawin, E. R., Ranganathan, R. & Horvitz, H. R. *C. elegans* locomotory rate is modulated by the
1190 environment through a dopaminergic pathway and by experience through a serotonergic pathway.
1191 *Neuron* **26**, 619-631 (2000).

1192 95 Pierce-Shimomura, J. T., Morse, T. M. & Lockery, S. R. The fundamental role of pirouettes in
1193 *Caenorhabditis elegans* chemotaxis. *Journal of Neuroscience* **19**, 9557-9569 (1999).

1194 96 Iino, Y. & Yoshida, K. Parallel use of two behavioral mechanisms for chemotaxis in *Caenorhabditis*
1195 *elegans*. *Journal of Neuroscience* **29**, 5370-5380 (2009).

1196 97 Miller, A. C., Thiele, T. R., Faumont, S., Moravec, M. L. & Lockery, S. R. Step-response analysis of
1197 chemotaxis in *Caenorhabditis elegans*. *Journal of Neuroscience* **25**, 3369-3378 (2005).

1198 98 Zariwala, H. A., Miller, A. C., Faumont, S. & Lockery, S. R. Step response analysis of thermotaxis in
1199 *Caenorhabditis elegans*. *Journal of Neuroscience* **23**, 4369-4377 (2003).

1200 99 Schimansky-Geier, L., Mieth, M., Rosé, H. & Malchow, H. Structure formation by active Brownian
1201 particles. *Physics Letters A* **207**, 140-146 (1995).

1202 100 Berg, H. C. *E. coli in Motion*. (Springer, 2004).

1203 101 Ibarra-Soria, X., Levitin, M. O., Saraiva, L. R. & Logan, D. W. The olfactory transcriptomes of mice.
1204 *PLoS genetics* **10**, e1004593 (2014).

1205 102 Kohl, J., Ostrovsky, A. D., Frechter, S. & Jefferis, G. S. A bidirectional circuit switch reroutes
1206 pheromone signals in male and female brains. *Cell* **155**, 1610-1623 (2013).

1207 103 Qiu, P. (2020).

1208 104 Bakken, T. E. *et al.* Single-nucleus and single-cell transcriptomes compared in matched cortical cell
1209 types. *PloS one* **13**, e0209648 (2018).

1210 105 Ziegenhain, C. *et al.* Comparative analysis of single-cell RNA sequencing methods. *Molecular cell*
1211 **65**, 631-643. e634 (2017).

1212 106 Jiang, R., Sun, T., Song, D. & Li, J. J. Statistics or biology: the zero-inflation controversy about scRNA-
1213 seq data. *Genome biology* **23**, 31 (2022).

1214 107 Ehrlich, A. T. *et al.* Expression map of 78 brain-expressed mouse orphan GPCRs provides a
1215 translational resource for neuropsychiatric research. *Communications Biology* **1**, 102 (2018).

1216 108 Gat, A. *et al.* Integration of spatially opposing cues by a single interneuron guides decision-making
1217 in *C. elegans*. *Cell Reports* **42** (2023).

1218 109 Page, J. L., Dickman, B. D., Webster, D. R. & Weissburg, M. J. Staying the course: chemical signal
1219 spatial properties and concentration mediate cross-stream motion in turbulent plumes. *Journal of*
1220 *Experimental Biology* **214**, 1513-1522 (2011).

1221 110 Gomez-Marin, A., Duistermars, B., Frye, M. A. & Louis, M. Mechanisms of odor-tracking: multiple
1222 sensors for enhanced perception and behavior. *Frontiers in cellular neuroscience* **4**, 1374 (2010).

1223 111 Borst, A. & Heisenberg, M. Osmotropotaxis in Drosophila melanogaster. *Journal of comparative*
1224 *physiology* **147**, 479-484 (1982).

1225 112 Budick, S. A. & Dickinson, M. H. Free-flight responses of Drosophila melanogaster to attractive
1226 odors. *Journal of experimental biology* **209**, 3001-3017 (2006).

1227 113 Taylor, S. R. *et al.* Molecular topography of an entire nervous system. *Cell* **184**, 4329-4347.e4323,
1228 doi:10.1016/j.cell.2021.06.023 (2021).

1229 114 Yemini, E. *et al.* NeuroPAL: a multicolor atlas for whole-brain neuronal identification in *C. elegans*.
1230 *Cell* **184**, 272-288. e211 (2021).

1231 115 Vidal, B. *et al.* An atlas of *Caenorhabditis elegans* chemoreceptor expression. *PLoS Biol* **16**,
1232 e2004218, doi:10.1371/journal.pbio.2004218 (2018).

1233 116 Pereira, L. *et al.* Timing mechanism of sexually dimorphic nervous system differentiation. *Elife* **8**,
1234 doi:10.7554/eLife.42078 (2019).

1235 117 Schindelin, J. *et al.* Fiji: an open-source platform for biological-image analysis. *Nature methods* **9**,
1236 676-682 (2012).

1237 118 Wolff, C. *et al.* Multi-view light-sheet imaging and tracking with the MaMuT software reveals the
1238 cell lineage of a direct developing arthropod limb. *Elife* **7**, e34410 (2018).

1239 119 Park, C. F. *et al.* Automated neuron tracking inside moving and deforming *C. elegans* using deep
1240 learning and targeted augmentation. *Nature Methods* **21**, 142-149 (2024).

1241 120 Berg, S. *et al.* Ilastik: interactive machine learning for (bio) image analysis. *Nature methods* **16**,
1242 1226-1232 (2019).

1243 121 Nava, S. *et al.* A cGAL-UAS bipartite expression toolkit for *Caenorhabditis elegans* sensory neurons.
1244 *Proceedings of the National Academy of Sciences* **120**, e2221680120 (2023).

1245 122 Pokala, N., Liu, Q., Gordus, A. & Bargmann, C. I. Inducible and titratable silencing of *Caenorhabditis*
1246 *elegans* neurons in vivo with histamine-gated chloride channels. *Proc Natl Acad Sci U S A* **111**,
1247 2770-2775, doi:10.1073/pnas.1400615111 (2014).

1248 123 Brinke, M., Heininger, P. & Traunspurger, W. A semi-fluid gellan gum medium improves nematode
1249 toxicity testing. *Ecotoxicology and Environmental Safety* **74**, 1824-1831 (2011).

1250 124 Fryer, E. *et al.* A high-throughput behavioral screening platform for measuring chemotaxis by *C.*
1251 *elegans*. *PLoS Biology* **22**, e3002672 (2024).

1252 125 Wan, X. & Sternberg, P. W. GelDrop Array High-Throughput Screening in Nematodes.
1253 *microPublication Biology* **10.17912/micropub.biology.001809** (2025).

1254 126 Lesanpezeshki, L. *et al.* Pluronic gel-based burrowing assay for rapid assessment of neuromuscular
1255 health in *C. elegans*. *Scientific reports* **9**, 15246 (2019).

1256 127 Beron, C. *et al.* The burrowing behavior of the nematode *Caenorhabditis elegans*: a new assay for
1257 the study of neuromuscular disorders. *Genes, Brain and Behavior* **14**, 357-368 (2015).

1258 128 Guisnet, A., Maitra, M., Pradhan, S. & Hendricks, M. A three-dimensional habitat for *C. elegans*
1259 environmental enrichment. *PLoS One* **16**, e0245139 (2021).

1260 129 Cao, M., Chai, C., Liu, J. & Sternberg, P. Application of the red-shifted channel rhodopsin Chrimson
1261 for the *Caenorhabditis elegans* cGAL bipartite system. *MicroPubl Biol* **2018**, doi:10.17912/2jgw-
1262 fj52 (2018).

130 Schild, L. C. & Glauser, D. A. Dual color neural activation and behavior control with chrimson and CoChR in *Caenorhabditis elegans*. *Genetics* **200**, 1029-1034 (2015).

131 Lu, Y. *et al.* Extrasynaptic signaling enables an asymmetric juvenile motor circuit to produce symmetric undulation. *Current Biology* **32**, 4631-4644. e4635 (2022).

132 Gower, J. C. Generalized procrustes analysis. *Psychometrika* **40**, 33-51 (1975).

133 Wood, S. N. Thin plate regression splines. *Journal of the Royal Statistical Society Series B: Statistical Methodology* **65**, 95-114 (2003).

134 Zhou, T. *et al.* AI-aided geometric design of anti-infection catheters. *Science Advances* **10**, eadj1741 (2024).

135 Chronis, N., Zimmer, M. & Bargmann, C. I. Microfluidics for in vivo imaging of neuronal and behavioral activity in *Caenorhabditis elegans*. *Nature methods* **4**, 727-731 (2007).

136 Pinkard, H. *et al.* Pycro-Manager: open-source software for customized and reproducible microscope control. *Nature methods* **18**, 226-228 (2021).

137 Appleby, P. A. The role of multiple chemotactic mechanisms in a model of chemotaxis in *C. elegans*: different mechanisms are specialised for different environments. *Journal of computational neuroscience* **36**, 339-354 (2014).

138 Wan, X. *et al*. Efficient pheromone navigation via antagonistic detectors. https://github.com/edmondztt/pheromone-traj-analysis. DOI: 10.5281/zenodo.18150733 (2024).

139 Wan, X. *et al*.. Source data_NCOMMS-25-63248 : Efficient pheromone navigation via antagonistic detectors in Caenorhabditis elegans male [Data set]. CaltechDATA. https://doi.org/10.22002/dp6gb-ky687(2026).

**Acknowledgments**

We are grateful to David Aguirre, Wilber Palma, Stephanie Nava, and Zachary Blumenfeld for their assistance during the early stages of this project. We acknowledge Natalie Sim and Elena Ruiz for data analysis. We also thank Helena Casademunt and Nicholas Markarian for their discussion and suggestions during the manuscript preparation. This work was supported by: R01 NS113119 (P.W.S., A.D.T.S.), Tianqiao and Chrissy Chen Institute for Neuroscience senior postdoc fellowship (X.W.), Tianqiao and Chrissy Chen Institute for Neuroscience postdoc innovator grant (X.W.) and Tianqiao and Chrissy Chen Institute for Neuroscience Systems Neuroscience Awards (P.W.S.). P.W.S. is Bren Professor of Biology. The *Caenorhabditis* Genetics Center provided some strains.

**Author Contributions**

X.W. and P.W.S. conceived the study and designed the experiments. X.W. and V.S. performed the behavioral assays, imaging, and optogenetics experiments. T.Z. and X.W. designed the computational model, performed the simulation and data analysis. X.W. and A.G. performed the microfluidics chip-based experiment. C.F.P. provided a whole-brain imaging data analysis platform. X.W., T.Z., and P.W.S. wrote the initial draft of the manuscript. All authors discussed the results and contributed to the final version of the manuscript. P.W.S., A.D.T.S., and J.F.B. supervised the project.

**Competing Interests Statement**

The authors have no conflicts of interest to disclose.

## Figures and Figure Legends

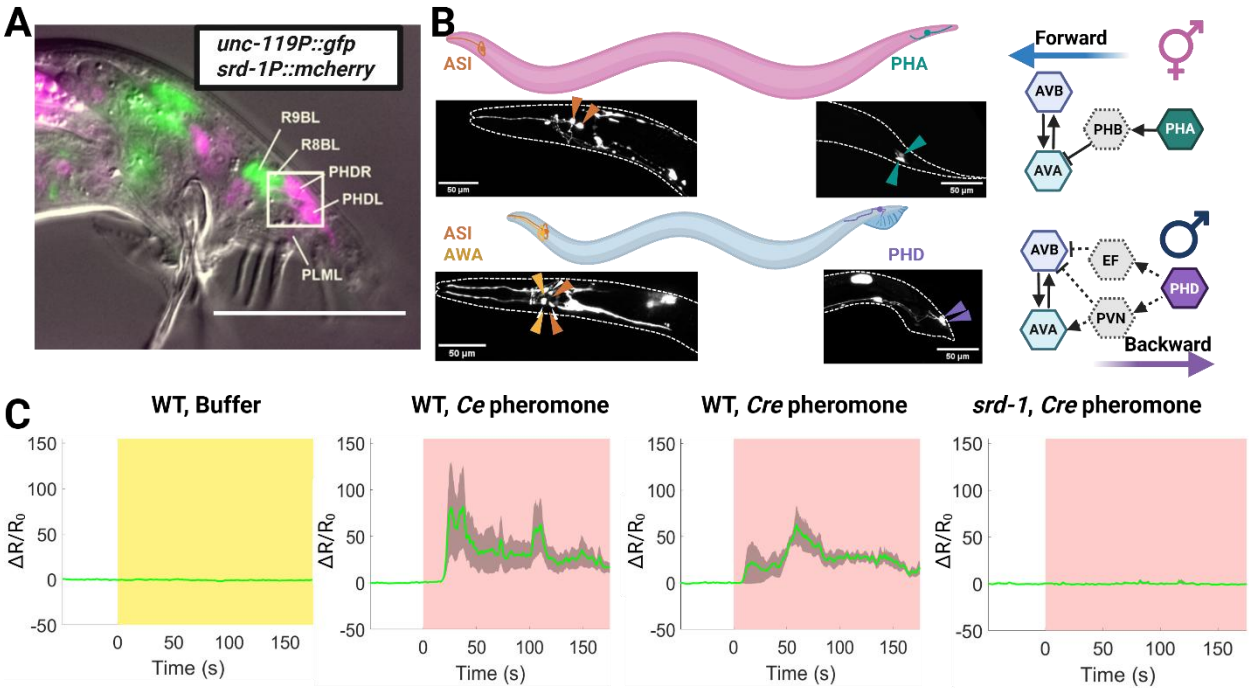


**Figure 1: *srd-1* sexual dimorphism in expression patterns and male PHD neuron excitation triggered by sex pheromone depends on the chemoreceptor SRD-1. (A)** Expression pattern of *srd-1*::mCherry (magenta pseudocolor) in male tail. *srd-1* is expressed in a pair of PHD cells located in tail region of male *C. elegans*. PHD neurons are defined based on their location in the tail ganglia, and its process morphology, with P*unc-119*::gfp indicating all neuronal cell bodies (green pseudocolor). SRD-1 is not expressed in Ray B neurons (Figure S1) as reported in the literature before the existence of PHD was known[70,71]. Scale bar, 50 µm. **(B)** Sexual dimorphic expression of *srd-1* in both head and tail: *srd-1* GFP reporter expression in AWAs, ASIs and male-specific neuron PHDs in males and in ASIs and PHAs in hermaphrodites. *rab-3P::mCherry* marks all neurons; an integrated cGAL-UAS line *(srd-1P*::GAL4; UAS::GFP*)* reports *srd-1* expression. The right panel shows the expression pattern summary of *srd-1* in both males and females, along with the predicted neural circuits it might be involved in, based on their connectome and functional connectome insights. Scale bars as indicated. **(C)** Sex pheromone-triggered activation of PHD neurons, exhibiting SRD-1-dependent excitation, was observed through pan-neuronal calcium imaging with *rgef-1P*::GCaMP6s; a pan-neural marker (*rgef-1P*::mNeptune) indicated all neuron cell body locations (sample size: 5-7 worms per condition). Shaded areas represent the s.e.m. White indicates the pre-stimulation stage and yellow shading indicates the time window of buffer application, while pink denotes the period of pheromone application. The green trace denotes the mean calcium ratio ($\Delta R/R_o$). The y-axis represents $\Delta R/R_o$, where R is defined as the fluorescence ratio of GCaMP to mNeptune. Created in BioRender. Wan, X. (2026) https://BioRender.com/9hzrztd. Source data are provided as a Source Data file.

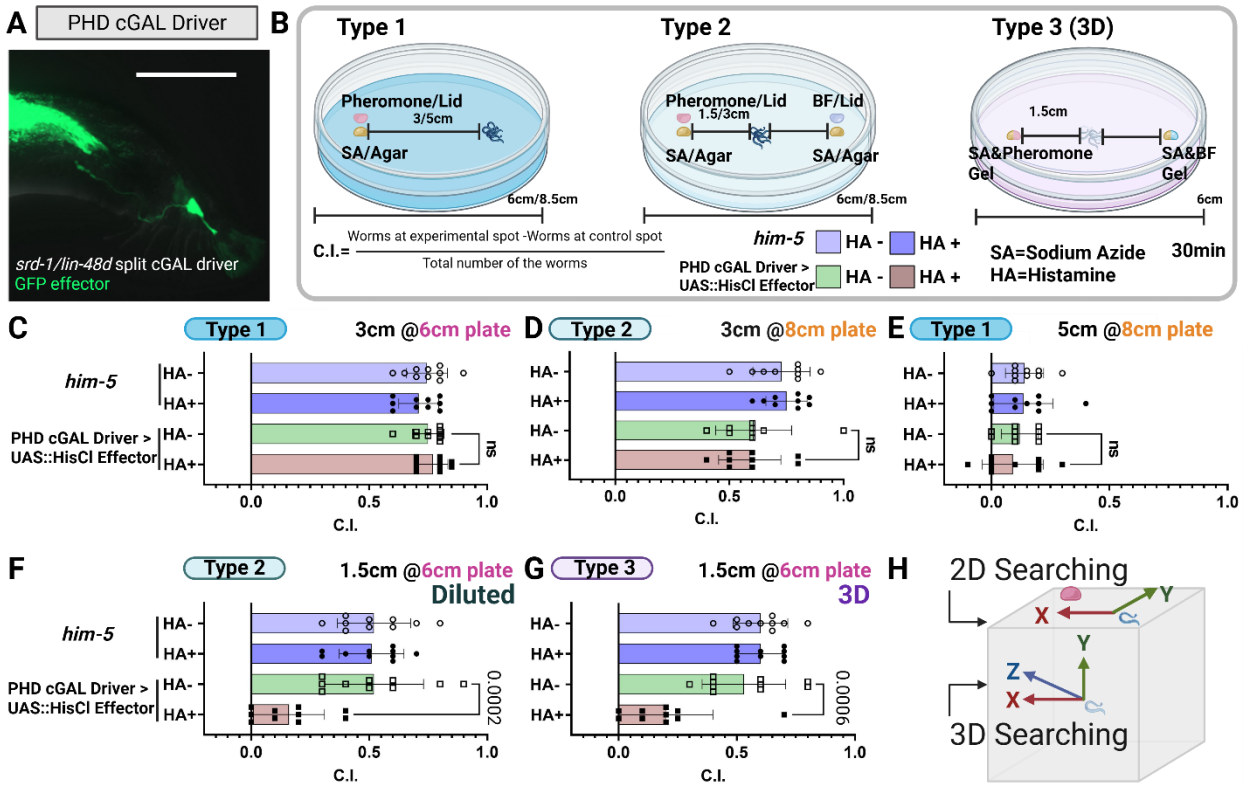


**Figure 2: Exploring the role of PHD neurons in mate-searching efficiency. (A)** Split cGAL construction of a PHD neurons-specific driver and validation of *srd-1* expression. Male tail fluorescence from *lin-48dP*::NLS::cGAL(DBD); *srd-1P*::NLS::cGAL(AD) crossed to 15×UAS::GFP demonstrates GFP labeling of PHD, verifying *srd-1* expression and providing a driver for targeted PHD manipulation. Scale bar, 50 µm. **(B)** Schematic representation of the chemoattraction assay and the calculation of the Chemoattraction Index (C.I.). **(C)-(G)** Impact of PHD inhibition on male mate-searching efficacy under varied task complexities. Males expressing *lin-48dP*::NLS::cGAL (DBD); *srd-1P*::NLS::cGAL (AD) (driver) × UAS::HisCl (effector) were inhibited by histamine to silence PHD. Controls were the same genotype without histamine treatment, and WT *him-5* with/without histamine treatment, as indicated. **(C)-(E)** Baseline chemotaxis: PHD-inhibited males locate sex pheromone comparably to controls in three tested conditions. **(E)** Sensitivity test (10× diluted pheromone): PHD inhibition significantly reduces detection and targeting performance. **(G)** 3D navigation (gellan gum/gel arena): PHD-inhibited males show impaired source finding relative to controls. The sample size for each assay consisted of 200 worms, 20 worms per trials, 10 trails. Not significant (ns): $P > 0.05$; exact P values are indicated on the figure. Two-tailed unpaired t-test. Error bars represent the s.e.m. **(H)** Schematic diagram of 2D (type 1 and 2) and 3D searching (type 3). Created in BioRender. Wan, X. (2026) https://BioRender.com/su7cm2k. Source data are provided as a Source Data file.

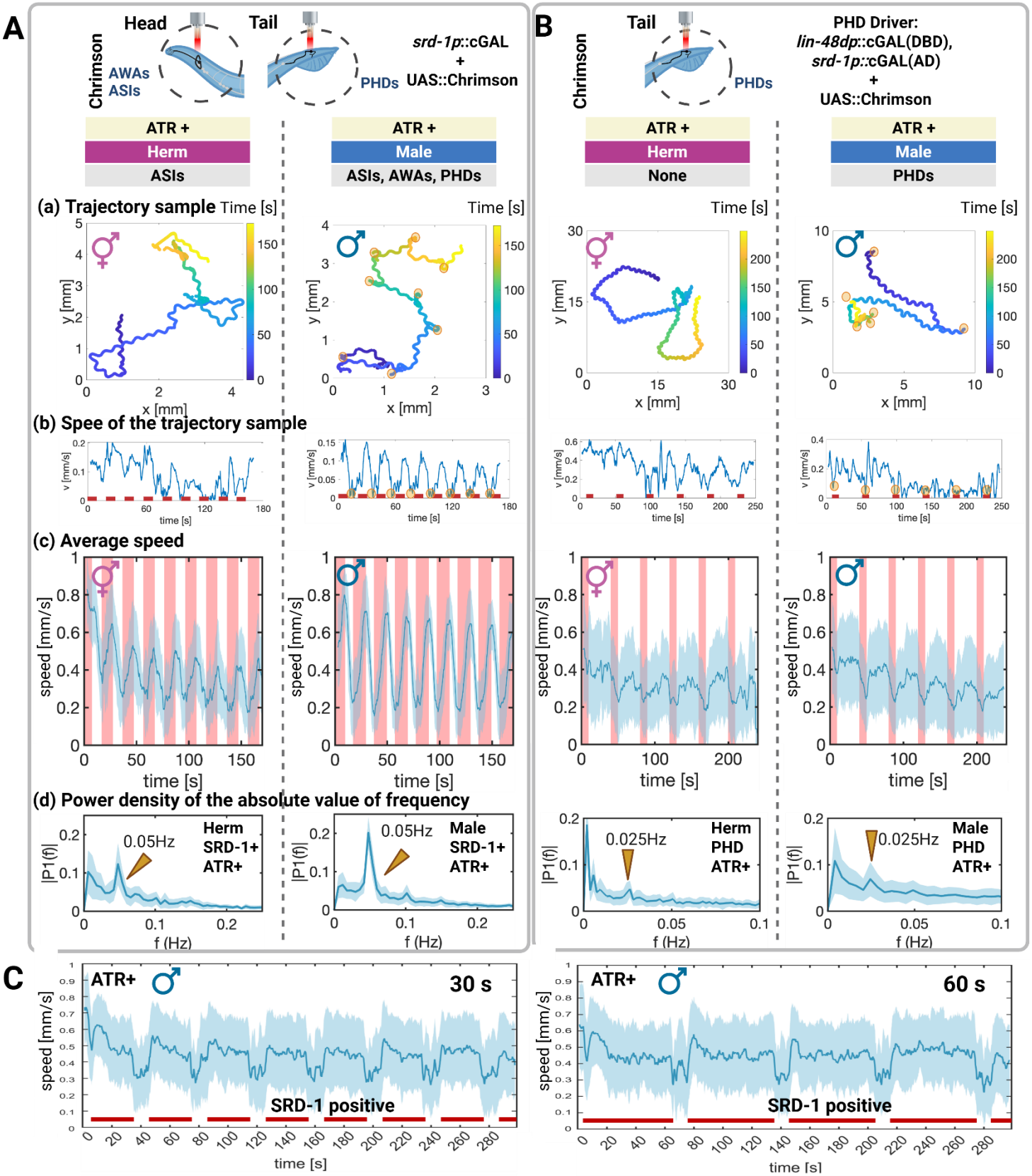
A
Head
Tail
Chrimson
AWAs
ASIs
PHDs
srd-1p::cGAL
+
UAS::Chrimson
ATR +
Herm
ASIs
ATR +
Male
ASIs, AWAs, PHDs
B
Tail
Chrimson
PHDs
PHD Driver:
lin-48dp::cGAL(DBD),
srd-1p::cGAL(AD)
+
UAS::Chrimson
ATR +
Herm
None
ATR +
Male
PHDs
(a) Trajectory sample
Time [s]
y [mm]
x [mm]
(b) Spee of the trajectory sample
v [mm/s]
time [s]
(c) Average speed
speed [mm/s]
time [s]
(d) Power density of the absolute value of frequency
|P1(f)|
f (Hz)
0.05Hz
Herm
SRD-1+
ATR+
Male
SRD-1+
ATR+
0.025Hz
Herm
PHD
ATR+
Male
PHD
ATR+
C
ATR+
30 s
60 s
SRD-1 positive
speed [mm/s]
time [s]

1350

**Figure 3: Contrasting locomotor responses to optogenetics activation of SRD-1 positive neurons and PHD neurons. (A)(B)** Schematic of optogenetics with region-specific genetic targeting: (A) head and tail region AWA, ASI and PHD neurons (*srd-1P*–cGAL > UAS::Chrimson) versus (B) tail PHD neurons (split cGAL: *lin-48dP*::NLS::cGAL[DBD]; *srd-1P*::NLS::cGAL[AD] > UAS::Chrimson). **(A)** Sex-specific locomotor responses to SRD-1 positive neuron activation in *C. elegans*. SRD-1 positive neurons (*srd-1P*-NLS-cGAL driver) were activated in both sexes using Chrimson (UAS::Chrimson effector). The stimulation protocol consisted of 12.5-second light-on intervals followed by 7.5-second light-off intervals, forming a 20-second cycle. Light stimulation is represented by the pink bar in the figure. Sample size: about 120 worms. **(B)** PHD neurons were activated by expressing Chrimson via a split-cGAL driver (*lin-48dP*::NLS::cGAL[DBD]; *srd-1P*::NLS::cGAL[AD]) crossed to 15×UAS::Chrimson; animals were treated with or without ATR and stimulated with light during the assay. ATR− and light-off served as negative controls. The stimulation protocol consisted of 10-second light-on intervals followed by 30-second light-off intervals, forming a 40-second cycle. Light stimulation is represented by the pink bar in the figure. The sample size for the SRD-1 positive neuron and PHD neuron activation assay included about 120 worms per sex. (See ATR- control in Figure S4) **(a, b)** A representative trajectory sample and its corresponding time series of instantaneous speed magnitude, total speed V(t), are shown. **(b)** The red line indicates periods of light stimulation. The yellow circle labeled all the turning events. **(c)** V(t) averaged over 120 worms. **(d)** Fourier analysis of V(t) from Fig. 3A–B demonstrates that optogenetic activation of SRD-1 positive neurons and PHD neurons produces expected peaks at 0.05 Hz and 0.025 Hz, corresponding to the 20-second and 40-second stimulation intervals, respectively. (c), (d) Shaded regions indicate ± s.d.; solid lines are means. **(C)** Persistent enhancement of forward movement upon activation of SRD-1 positive neurons, sustained for up to 60 seconds. The stimulation protocol involved 30- or 60-second light-on intervals followed by 10-second light-off intervals. Sample size: 100 (30s stimulation) and 110 (60s stimulation) worms. Pink/red bars indicate periods of light stimulation. Shaded regions indicate ± s.d.; solid lines are means. Created in BioRender. Wan, X. (2026) https://BioRender.com/lsxa7k1. Source data are provided as a Source Data file.

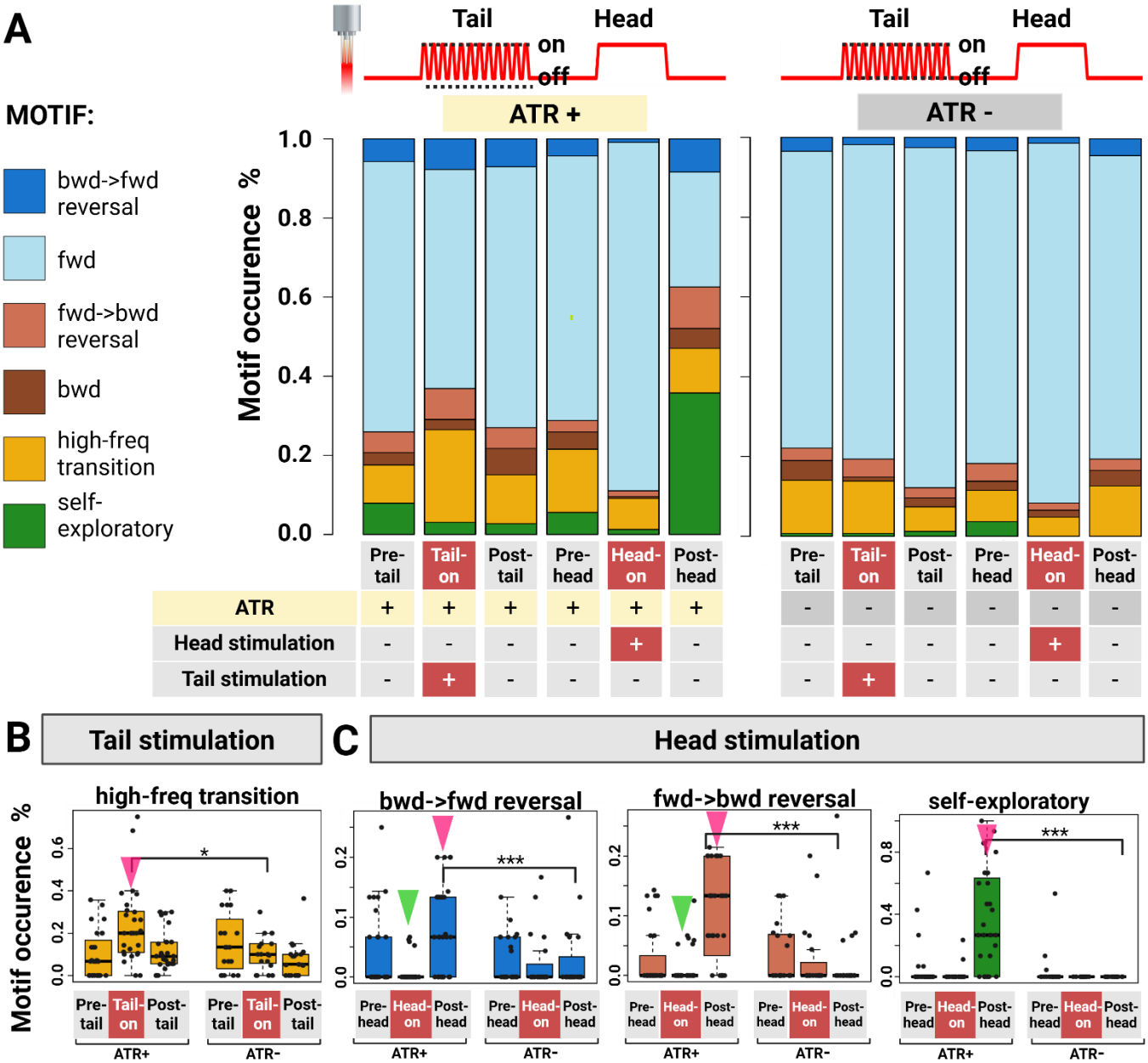
A
Tail
Head
on
off
ATR +
ATR -
MOTIF:
bwd->fwd reversal
fwd
fwd->bwd reversal
bwd
high-freq transition
self-exploratory
Motif occurence %
1.0
0.8
0.6
0.4
0.2
0.0
Pre-tail
Tail-on
Post-tail
Pre-head
Head-on
Post-head
ATR
Head stimulation
Tail stimulation
B
Tail stimulation
C
Head stimulation
high-freq transition
bwd->fwd reversal
fwd->bwd reversal
self-exploratory
ATR+
ATR-

**Figure 4: Six-Motif Analysis: Characterizing micro-behavioral responses to optogenetic stimulation of SRD-1 positive neurons in male *C. elegans*' anterior and posterior regions. (A)** Summary of all characterized micro-behavioral and their portion among all behaviors. With *srd-1* drivers and Chrimson effectors in cGAL-UAS lines (*srd-1P*–cGAL > UAS::Chrimson) combined with region-specific light sources, we precisely targeted the head (AWAs and ASIs) or tail regions (PHDs) of freely moving males to analyze locomotion effects and characterize specific micro-behaviors. Behavioral segments were classified in 2-s windows as forward (fwd), backward (bwd), fwd-bwd reversal, bwd-fwd reversal, high-frequency direction transitions, or self-exploratory. High-frequency direction transitions, defined as >2 direction changes within a 2-s window, reflecting an exploratory strategy that cannot be unambiguously assigned to fwd-bwd or bwd-fwd. Self-exploratory, in which the worm engages in near-body probing behavior. **(B)** Tail-restricted illumination increases high-frequency transitions during light stimulation. All animals carried *srd-1P*–cGAL > 15×UAS::Chrimson and were reared ± all-trans-retinal (ATR). To probe tail-region circuits (PHDs), we delivered posterior-restricted light (illumination geometry and parameters in Methods). During light-on, ATR+ animals exhibited a robust increase in high-frequency direction transitions; this effect was absent in ATR− controls and in light-off trials. Behavior returned toward baseline after light-off. **(C)** Head-restricted illumination suppresses transitions during light stimulation and promotes transitions and self-exploration after light-off. Using the same *srd-1P*–cGAL > UAS::Chrimson genotype, we applied head-restricted light to engage head-region circuits (including AWAs/ASIs). In ATR+ animals, light-on suppressed direction transitions (both bwd-fwd and fwd-bwd). Following light-off, both transitions rebounded above baseline, and animals displayed increased self-exploratory "body-probing" behavior (tail pressed against/near the body). No significate changes were observed in ATR− or light-off controls. **(A)-(C)** The sample size for ATR+ group consisted of 18 worms. The sample size for ATR- group consisted of 12 worms. Green arrows indicate decreases in the $ATR^{+}$ group during stimulation relative to pre-stimulation, post-stimulation, and $ATR^{-}$ group levels during stimulation. Pink arrows represent increases relative to the same conditions. ***$P < 0.001$; **$P < 0.005$; *$P < 0.05$. **(B)-(C)** Box plots indicate the median (center line); lower/upper box bounds are the 25th and 75th percentiles; whiskers extend to the minimum and maximum data points. Source data are provided as a Source Data file.

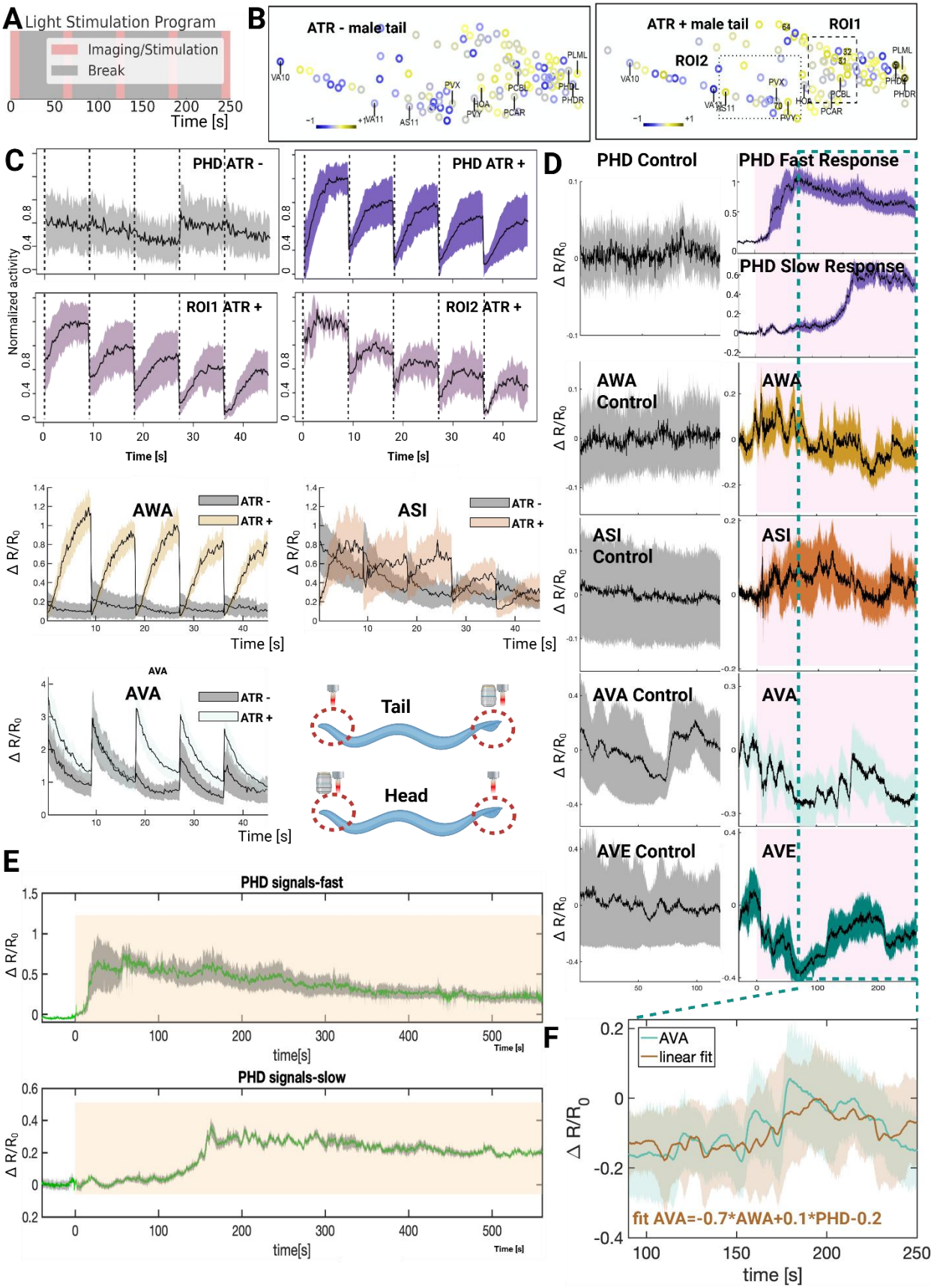
A
Light Stimulation Program
Imaging/Stimulation
Break
Time [s]
B
ATR - male tail
ATR + male tail
ROI1
ROI2
C
PHD ATR -
PHD ATR +
ROI1 ATR +
ROI2 ATR +
Normalized activity
Time [s]
AWA
ASI
AVA
ATR -
ATR +
Δ R/R0
Tail
Head
D
PHD Control
PHD Fast Response
PHD Slow Response
AWA Control
AWA
ASI Control
ASI
AVA Control
AVA
AVE Control
AVE
E
PHD signals-fast
PHD signals-slow
time[s]
F
AVA
linear fit
fit AVA=-0.7*AWA+0.1*PHD-0.2
time [s]

1453

**Figure 5: neural activation and correlation patterns following *srd-1* positive neuron optogenetic stimulation and pheromone exposure. (A)** Schematic representation of the optogenetic activation protocol, consisting of five 10-second imaging/stimulation intervals interspersed with 50-second breaks. **(B)-(C)** For optogenetic activation and calcium imaging we expressed Chrimson by crossing an *srd-1P*::Gal4(sk)::VP64 driver to a 15×UAS::Chrimson effector in the pan-neuronal imaging background. Animals were reared ± ATR, and defined light stimuli were delivered during imaging; Chrimson-dependent responses were observed only in ATR+ light-on trials. **(B)** Representative activation patterns were observed in male tail neurons. Through visual analysis, two regions, designated as ROI1 and ROI2, were identified as containing neurons with strong correlations to PHD activity (correlation coefficient >0.55) (See Figure S6 and S7). The sample sizes: control (n=9) and experimental (n=12). **(C)** Traces of neuronal activities in PHD neurons and in two regions (ROI1 and ROI2) which often contain neurons strongly correlated with PHD. The sample sizes: control (n=9) and experimental (n=12) (See Figure S6 and S7). Third and Forth row: neuronal activation in male head regions after optogenetic activation of all SRD-1 positive neurons; sample sizes: control and experimental groups (n=8 each, See Figure S9). **(D)-(F)** Pheromone odor stimulation and calcium imaging. All panels use the pan-neuronal imaging strain and are exposed to volatile sex-pheromone extract; stimulus and the delivery method/protocol are detailed in Methods. **(D)** Calcium responses in PHD, AWA, ASI, and reversal commanding neurons AVA and AVE upon 250 seconds of pheromone stimulation in both tail and head regions. Sample sizes for both regions are control (n=5) and experimental (n=8). **(E)** Calcium responses of PHD neurons over 9.5 mins of pheromone stimulation, with data grouped by response initiation time into two categories. The sample sizes are 13 worms. (B), (C), and (E) Shaded areas represent the s.e.m. **(F)** Fitting AVA neural activity data using a linear combination of AWA and PHD neural activity, focusing on the period both AWA and PHD neurons activated. This model indicates a weighted influence of AWA and PHD neuron activities on AVA neuronal response. Shaded regions indicate ± s.d.; solid lines are means. Created in BioRender. Wan, X. (2026) https://BioRender.com/lsxa7k1. Source data are provided as a Source Data file.

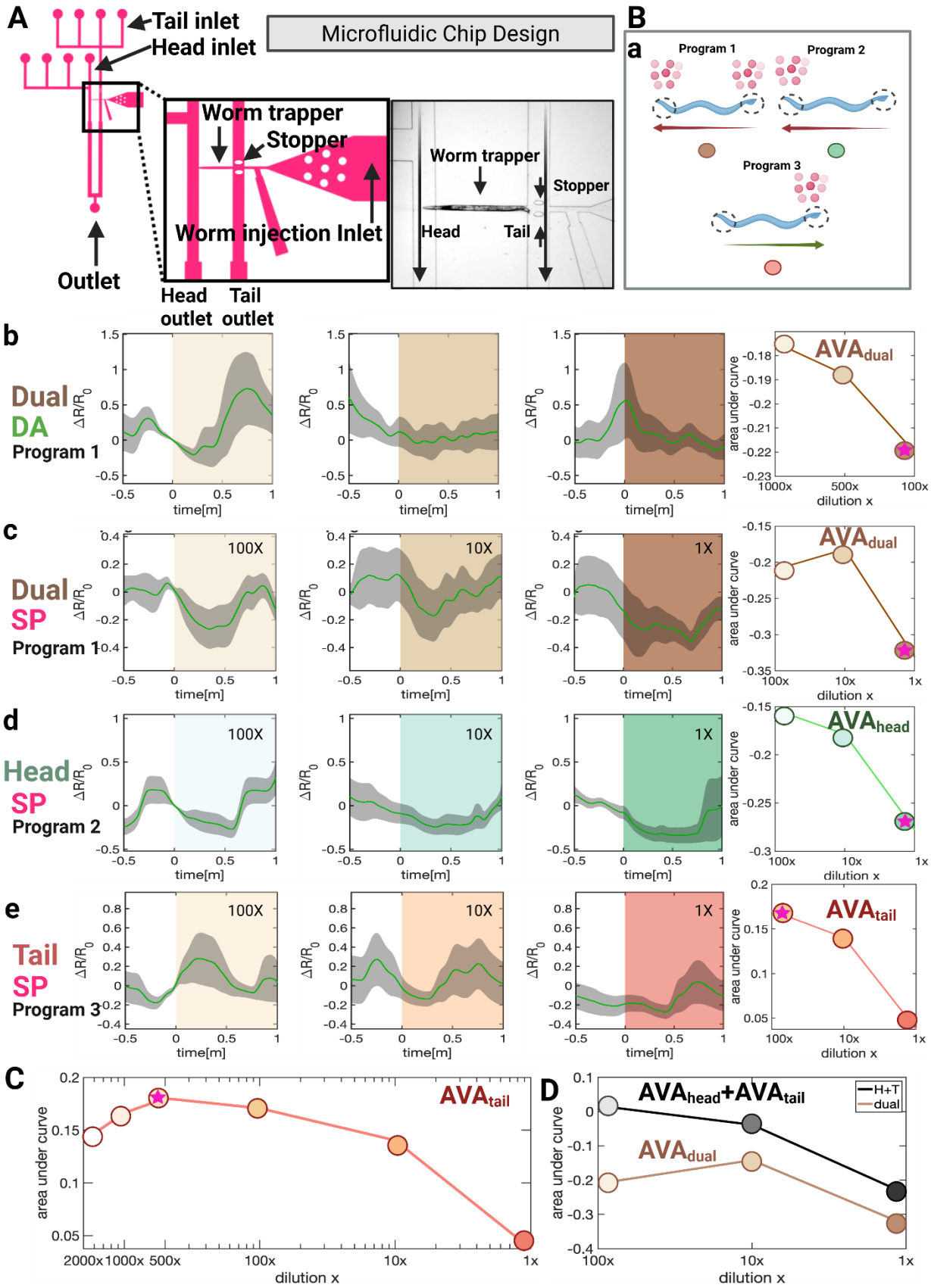
A
Tail inlet
Head inlet
Microfluidic Chip Design
Worm trapper
Stopper
Worm injection Inlet
Outlet
Head outlet
Tail outlet
Worm trapper
Stopper
Head
Tail
B
a
Program 1
Program 2
Program 3
b
Dual
DA
Program 1
c
Dual
SP
Program 1
d
Head
SP
Program 2
e
Tail
SP
Program 3
100X
10X
1X
ΔR/R0
time[m]
area under curve
dilution x
AVAdual
AVAhead
AVAtail
C
D
AVAhead+AVAtail
AVAdual
H+T
dual

1499

**Figure 6: Dissecting reversal command neuron responses across different sex pheromone concentrations by microfluidics chip-based experiment (A)** Schematic of the head and tail microfluidic chip designed for precise, independent delivery of target concentration stimuli to the head and tail regions separately (See Method). **(B) (a)** Schematic diagram of stimulation program and predicted behavioral outcomes. **(b)-(e)** Effects of diacetyl and sex pheromone stimulation on AVA reversal command interneuron activity in *C. elegans* males. The calcium indicator GCaMP6s was used to monitor calcium dynamics in the AVA neuron. The AVA-specific split cGAL driver construct consisted of *gpa-14P*::NLS::cGAL (DBD)::gp41-1::N-intein::*let-858* 3'UTR and *rig-3P*::NLS::gp41-1::C-intein::cGAL(AD)::*let-858* 3'UTR, paired with the GCaMP effector construct 15xUAS::GCaMP7b::SL2::mKate2. Diacetyl and dual-sided sex pheromone stimulation reduce AVA activity, as does head-specific pheromone stimulation, whereas tail-specific pheromone stimulation activates AVA neurons. Shaded areas represent the standard error of the mean (s.e.m.). The right panel shows area-under-curve (AUC) analysis (see Method), indicating that dual-sided diacetyl and sex pheromone stimulation, as well as head-specific pheromone stimulation, exert the strongest inhibitory effects on AVA at the highest tested concentration. Tail-specific pheromone stimulation produces peak AVA activation at the lowest tested concentration (100-fold dilution). **(C)** Further testing of three additional diluted concentrations reveals that tail-specific stimulation elicits the highest activation of the AVA neuron at an intermediate concentration (500-fold dilution), with activation levels decreasing at both higher and lower concentrations. Each condition (head, tail, or dual location) at each concentration was tested with a sample size of 8 worms. **(D)** The area under the curve (AUC) for AVA neuron activation resulting from head-specific stimulation combined with tail-specific stimulation closely matches the trend observed with dual stimulation alone. The hot pink star indicates the concentration that resulted in the highest inhibitory or activating effect on AVA neurons. Created in BioRender. Wan, X. (2026) https://BioRender.com/5ttxkvk. Source data are provided as a Source Data file.

1538

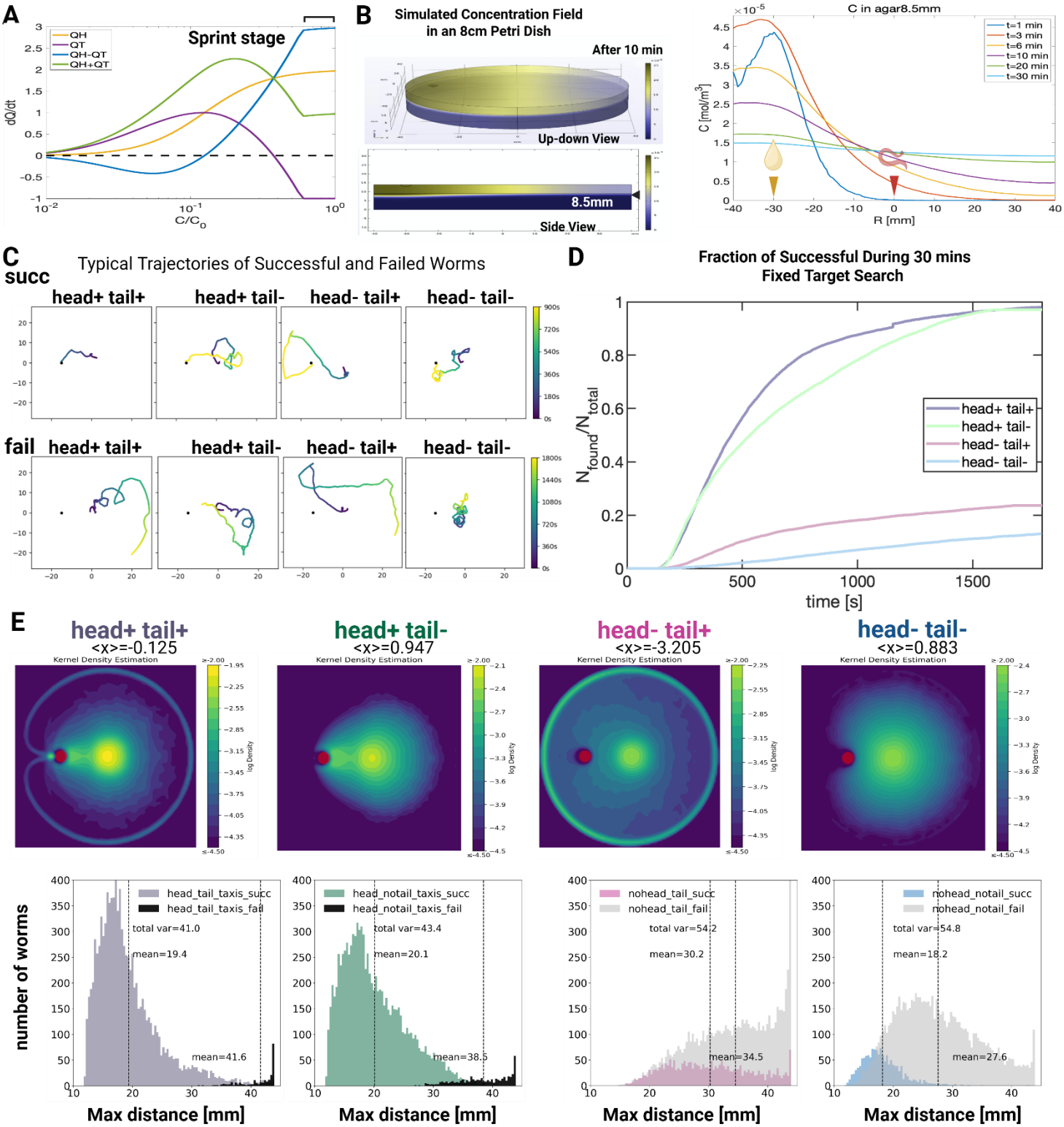
A
Sprint stage
QH
QT
QH-QT
QH+QT
dQ/dt
C/C0
B
Simulated Concentration Field
in an 8cm Petri Dish
After 10 min
Up-down View
8.5mm
Side View
C in agar8.5mm
t=1 min
t=3 min
t=6 min
t=10 min
t=20 min
t=30 min
C [mol/m3]
R [mm]
C
succ
Typical Trajectories of Successful and Failed Worms
head+ tail+
head+ tail-
head- tail+
head- tail-
fail
D
Fraction of Successful During 30 mins
Fixed Target Search
Nfound/Ntotal
time [s]
E
head+ tail+
<x>=-0.125
head+ tail-
<x>=0.947
head- tail+
<x>=-3.205
head- tail-
<x>=0.883
Kernel Density Estimation
log Density
number of worms
head_tail_taxis_succ
head_tail_taxis_fail
total var=41.0
mean=19.4
mean=41.6
head_notail_taxis_succ
head_notail_taxis_fail
total var=43.4
mean=20.1
mean=38.5
nohead_tail_succ
nohead_tail_fail
total var=54.2
mean=30.2
mean=34.5
nohead_notail_succ
nohead_notail_fail
total var=54.8
mean=18.2
mean=27.6
Max distance [mm]

1539

**Figure 7: Dynamic model for a navigation mechanism with antagonistic detectors. (A)** Schematic plot illustrating how confidence change rates depend on absolute concentration $C$ in the model. $C_0$ is the reference concentration at the pheromone source. For head input $Q^H$, a fixed concentration change rate is assumed for the sensory input. At low $C$, both head ($Q^H$) and tail ($Q^T$) inputs accumulate slowly. At intermediate $C$, tail input accumulates faster than head input. At higher $C$, tail input accumulates slower and is eventually suppressed, while head input signal is monotonically stronger as $C$ increases until saturation at very high $C$. The high $C$ regime corresponds to a large $Q^H - Q^T$ which leads to the sprint behavior. **(B)** Left panel: the simulated concentration field within an 8-cm Petri dish 10 mins after stimulus introduction. The stimulus is on the lid of a plate half-filled with agar (9mm thickness), establishing a dual-layer distribution for the volatile component. The black arrowhead marks the layers' interface in the bottom panel. Right panel: evolution of the concentration field at the air and agar interface (8.5mm) over a 30-minute duration. **(C-E)** Simulation results. **(C)** Typical trajectories of successful and failed subgroups under different conditions of head/tail inhibition. **(D)** Fraction of worms that have found source during 30min search task under each condition. Tail activation results in slightly better performance for head-activated worms (compare purple and green curves) and about twice better for head-inhibited worms (compare blue and grey curves). No taxis happen under head inhibition. **(E)** The upper panels show the simulated spatial distributions of worms averaged over 30 mins. The red dot shows the location of the pheromone source, and all worms start at an average distance of 15 mm to the right side of the pheromone source. <x> is the mean position along the horizontal direction. The bottom panels show the histogram (Y-axis) of the maximum distance (X-axis) from the pheromone source that worms reached. Simulation sample size=10000 for each of the four different conditions. The mean of maximum distance and total variance are indicated in each panel. Created in BioRender. Wan, X. (2026) https://BioRender.com/5ttxkvk. Source data are provided as a Source Data file.

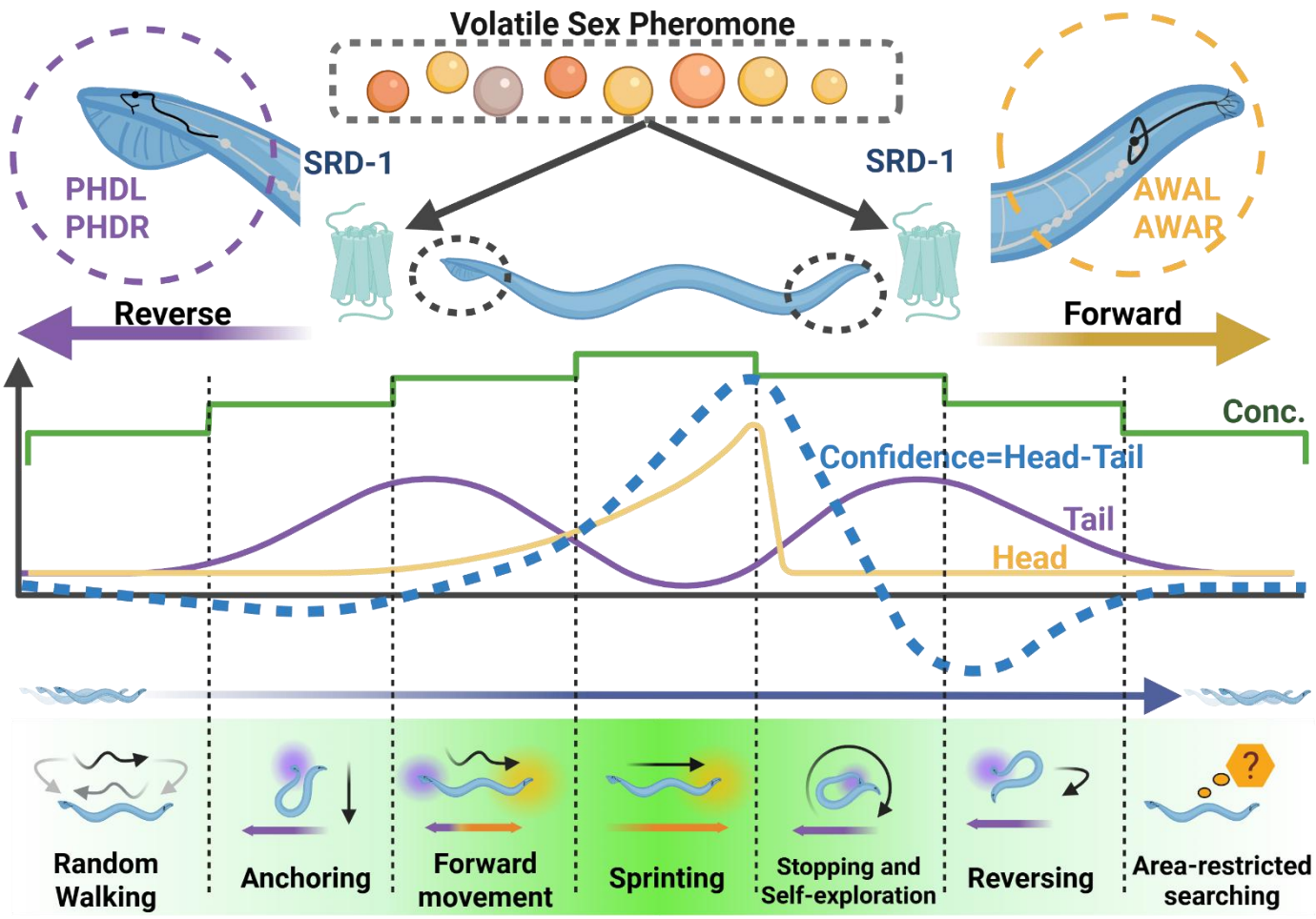


**Figure 8: Spatially separated pheromone detection drives adaptive navigation in *C. elegans* males.**

The **upper panel** illustrates how *C. elegans* males utilize spatially separated pairs of sensory neurons, AWA (head) and PHD (tail), that detect the same volatile sex pheromone molecule via the receptor SRD-1. Despite sharing this receptor, head neurons detect gradient changes and activate when concentration increases, suppressing turning, and promoting forward movement and acceleration. In contrast, tail neurons detect absolute concentration and activate at preferred moderate concentrations, inducing reversals and deceleration. The **bottom panel** shows that upon initial pheromone introduction, simultaneous activation of head and tail neurons cancels each other out, causing males to transition from random walking to a stationary anchoring state, preventing them from chasing the concentration wave initially. As pheromone concentration increases, head neurons dominate, driving forward locomotion and acceleration. At the highest concentrations, tail neurons become less active while head neurons are highly activated, leading to rapid, goal-directed movement (sprinting). Incorrect directional choices result in AWA deactivation and persistent PHD activity, inducing pausing and local exploration. Repeated unsuccessful attempts trigger area-restricted searching. Created in BioRender. Wan, X. (2026) https://BioRender.com/5ttxkvk.